



# Retrieval of SO<sub>2</sub> columns from FY3F/OMS instrument observations

Huanhuan Yan<sup>1</sup>, Andreas Richter<sup>2</sup>, Xingying Zhang<sup>1\*</sup>, Anja Schönhardt<sup>2</sup>, Thomas Visarius<sup>2</sup>

<sup>1</sup>Key Laboratory of Radiometric Calibration and Validation for Environmental Satellites, National Satellite Meteorological Center (National Center for Space Weather), Innovation Center for FengYun Meteorological Satellite, Beijing, 100081, China.

<sup>2</sup>Institute of Environmental Physics (IUP-UB), University of Bremen, Bremen, 28359, Germany.

*Correspondence to:* Xingying Zhang (zxy@cma.gov.cn)

**Abstract.** Atmospheric SO<sub>2</sub> has a significant impact on the urban environment and on global climate. Remote sensing provides an unprecedented tool for the continuous and real-time monitoring of atmospheric SO<sub>2</sub> from volcanic eruptions and anthropogenic emissions. The Ozone Monitoring Suite (OMS) onboard the Chinese FENGYUN-3F (FY-3F) satellite launched in August 2023 is a new hyperspectral UV-VIS instrument in the FY-3 family of satellites, aiming to obtain information about atmospheric trace gases. In this study, we use the OMS Nadir (OMS-N) top-of-atmosphere (TOA) measurements and Differential Optical Absorption Spectroscopy (DOAS) inversion to for the first time retrieve global SO<sub>2</sub> columns from these measurements. Based on the characteristics of the OMS instrument and the performance of its L1 data, specific schemes including solar spectrum selection, spectral soft calibration, and background offset correction were developed to effectively reduce along-track stripes and across-track asymmetry found in the initial OMS SO<sub>2</sub> retrievals. The accuracy of FY-3F/OMS SO<sub>2</sub> retrievals was evaluated by comparing them with the DOAS and COvariance-Based Retrieval Algorithm (COBRA) SO<sub>2</sub> products from the TROPOspheric Monitoring Instrument (TROPOMI) onboard Copernicus Sentinel-5 Precursor (Sentinel-5P) over three typical areas: clean oceanic regions, volcanic eruption regions, and anthropogenic emission regions. The results indicate that the OMS SO<sub>2</sub> retrievals exhibit good stability over clean oceanic regions, successfully capture volcanic SO<sub>2</sub> plumes, and effectively detect the elevated SO<sub>2</sub> columns from anthropogenic emissions in regions such as the Middle East, Eastern India, and Northern Russia. Air mass factor (AMF) uncertainty remains the primary error source of this first version of OMS SO<sub>2</sub> retrievals. This study is the first to present SO<sub>2</sub> retrievals from FY3F/OMS observations, which is crucial for a comprehensive understanding of OMS's capability in SO<sub>2</sub> retrievals.

## 1 Introduction

Sulfur dioxide (SO<sub>2</sub>) is a short-lived trace gas in the atmosphere that affects regional air quality and global climate change. SO<sub>2</sub> is primarily released by anthropogenic activities (e.g., smelting of sulfur ore, combustion of coal, the oil and gas industry, emissions of motor vehicles) and natural phenomena (e.g., volcanic and biological processes) (Finlayson-Pitts and Pitts Jr, 1999; Cullis and Hirschler, 1980; Seinfeld and Pandis, 2016). SO<sub>2</sub> injection from a volcanic eruption can reach up to the upper troposphere/lower stratosphere, not only affecting global climate but also posing a threat to aviation, along with



volcanic ash. Through reaction with hydroxide and water, atmospheric SO<sub>2</sub> can be rapidly converted into sulfate aerosols. These aerosols both scatter and absorb solar and terrestrial radiation, affecting the radiation balance of the atmosphere (cooling or warming effect) (Twomey, 1977). Sulfate particles formed from anthropogenic SO<sub>2</sub> emissions not only influence atmospheric visibility in the boundary layer but also contribute to acid rain which in turn damages ecosystems.

35 Satellite remote sensing offers the advantages of near global coverage, short-term periodic observation capabilities, and continuous spatial coverage. Due to the strong absorption characteristics of SO<sub>2</sub> in the ultraviolet (UV) spectrum, especially in the 300–400 nm wavelength range, atmospheric SO<sub>2</sub> information can be obtained from the reflected TOA radiance spectrum. Since the first UV-based satellite observation of large amounts of SO<sub>2</sub> from the El Chichón volcanic eruption in 1982 by TOMS (Krueger, 1983), hyperspectral UV satellite instruments have been used to quantitatively monitor the spatial  
40 and temporal distribution of SO<sub>2</sub> concentrations and diffusion trends before and after volcanic eruptions. This compensates for the limitations of ground-based measurements, such as the high cost of dense in-situ observation networks and instrument maintenance (Krueger, 1983; Carn et al., 2005; Carn et al., 2007; Carn et al., 2009).

With the launch of a series of hyperspectral UV detection instruments, including the Global Ozone Monitoring Experiment (GOME) (Burrows et al., 1999; Khokhar et al., 2005; Eisinger and Burrows, 1998), the Scanning Imaging Absorption  
45 Spectrometer for Atmospheric Cartography (SCIAMACHY) (Gottwald and Bovensmann, 2010; Richter et al., 2006), the Ozone Monitoring Instrument (OMI) (Levelt et al., 2006), the Global Ozone Monitoring Experiment-2 (GOME-2) (Heue et al., 2010; Munro et al., 2006; Richter, 2009), the Ozone Mapping and Profiler Suite (OMPS) (Yang et al., 2013; Flynn et al., 2006), TROPOMI (Theys et al., 2019; Voors et al., 2017; Veeckind et al., 2012), and the Environmental Trace Gas Monitoring Instrument (EMI) (Chen et al., 2021; Zhao et al., 2020; Yan et al., 2021), satellite detection has been widely  
50 applied to monitor global SO<sub>2</sub> variations and to support research on climate change, atmospheric chemistry, and the atmospheric environment.

FY3F/OMS is a newly launched Chinese UV-VIS hyperspectral sensor that provides global observations with 7 km × 7 km spatial resolution at nadir and a morning overpass time. For a thorough understanding of the OMS SO<sub>2</sub> product, this study presents OMS SO<sub>2</sub> retrievals by using the OMS measurements and DOAS inversion, and compares them with TROPOMI  
55 DOAS and TROPOMI COBRA SO<sub>2</sub> products over clean oceanic regions, volcanic eruption regions, and anthropogenic emission regions. This paper is organized as follows. Section 2 gives a brief introduction to the FY3F/OMS instrument. Section 3 describes the detailed procedures used to retrieve the SO<sub>2</sub> columns from FY3F/OMS observations, including solar spectrum selection, spectral soft calibration, SO<sub>2</sub> slant column density (SCD) retrieval, background offset correction, and the simplified approach for AMF calculation used. Section 4 provides the OMS SO<sub>2</sub> column results, followed by comparisons  
60 with the TROPOMI DOAS and TROPOMI COBRA SO<sub>2</sub> products. Section 5 discusses error sources of OMS SO<sub>2</sub> retrievals, including the instrument-related errors and DOAS SCD spectral fitting errors in OMS SO<sub>2</sub> SCD retrievals, errors introduced by the simplified AMF approach taken, and the residual errors after background offset correction. The last section summarizes the main results and offers conclusions, along with suggestions for future improvements.



2 The FY3F/OMS Instrument

65 The FY-3F satellite, the 21st in China’s FengYun series, was successfully launched on August 3, 2023. It operates in a sun-synchronous orbit at an altitude of 836 km, with a descending node equatorial overpass time of 10:00 AM. Equipped with 10 advanced atmospheric instruments, FY-3F is designed to provide high-quality data for weather forecasting, climate monitoring, and environmental research, contributing significantly to global meteorological and environmental observations. The Ozone Monitoring Suite (OMS) onboard FY-3F satellite is a new instrument in the FY-3 family of satellites. It has two observation modes: Nadir (OMS-N) and Limb (OMS-L) (Wang et al., 2024). While OMS-L provides information on the vertical distribution of O<sub>3</sub>, OMS-N is mainly used to obtain column information on trace gases such as O<sub>3</sub>, NO<sub>2</sub>, SO<sub>2</sub>, and HCHO, and aerosols, as well as vertical profiles of O<sub>3</sub>. OMS-N operates using a push-broom observation technique to obtain daily global measurements, with a wide Field of View (FOV) of 112 °, covering three spectral bands: UV1 (250-300 nm), UV2 (300-320 nm), and VIS (307-493 nm). To enhance the signal-to-noise ratio (SNR) of the original detector rows, sets of 16 pixels are averaged to yield 58 spatial rows in the UV1 band, and four pixels are averaged to acquire 238 spatial rows in the UV2 and VIS bands, respectively (Wang et al., 2024). The OMS-N VIS band (307-493 nm) was used for the retrieval of OMS SO<sub>2</sub> columns in this study. It has a high spatial resolution of 7 km x 7 km at the nadir point, with a spectral resolution of 0.5-0.6 nm (Table 1). FY3F/OMS data can be downloaded from the website <http://data.nsmc.org.cn/DataPortal/en/home/index.html>.

80

Table1. The main characteristics of the FY3F/OMS-N instrument

Parameter	Nadir column measurement	Nadir profile measurement
Spectral range	VIS: 307~493nm	UV1:250~300nm UV2: 300~320nm
Spectral resolution	0.5~0.6nm	UV1: ~1.0nm UV2: ~0.5nm
Spectral accuracy	0.01nm	0.05nm
Spatial resolution at nadir point	7 km x 7 km	UV1: 21 km x 28 km UV2: 7 km x 7 km
Atmospheric products	O <sub>3</sub> , NO <sub>2</sub> , SO <sub>2</sub> , HCHO, AOD, cloud fraction and pressure	O <sub>3</sub> profile
Field of view	112 °	
Orbit observation	polar sun synchronous morning orbit	
Orbit altitude	836 km	
Equator crossing time	10:00 AM	
Duty Cycle	Daytime only	
Revisit Time:	24 hours	



### 3 SO<sub>2</sub> column retrievals from FY3F/OMS

The SO<sub>2</sub> retrieval from FY3F/OMS mainly involves the following steps. Firstly, the OMS-N L1 earth radiance is normalized to the Earth-Sun distance of 1AU, while the solar irradiance is obtained by convolving the Total and Spectral Solar Irradiance Sensor (TSIS) Hybrid Solar Reference Spectrum (HSRS) (Coddington et al., 2021) (See section 3.1 for more information) with the Instrument Spectral Response Function (ISRF) of OMS-N. Secondly, the 312-326 nm region is chosen as the retrieval fitting window of the OMS SO<sub>2</sub> column. Thirdly, spectral soft calibration is performed using the absorption peaks and valleys of the solar reference spectrum. Fourthly, the cross sections of SO<sub>2</sub> and O<sub>3</sub> in 312-326 nm are convolved with the ISRF. Fifthly, the Ring spectrum is calculated using the SCIATRAN Radiative Transfer Model (Rozanov et al., 2005). Sixthly, SO<sub>2</sub>, O<sub>3</sub> and Ring cross-sections together with a third-order polynomial are used in the DOAS fitting process to obtain the SCD of OMS SO<sub>2</sub>. Seventhly, the AMF is applied to get vertical column density (VCD). Finally, a specific correction scheme for OMS background offset is applied to effectively reduce along-track stripes and across-track asymmetries in the initial OMS SO<sub>2</sub> retrievals. It should be noted that, due to the current unavailability of synchronized and reliable OMS cloud and aerosol products, the effects of clouds and aerosol on SO<sub>2</sub> retrievals were not considered in this study. For the OMS SO<sub>2</sub> product, it is recommended to use retrieval results with a solar zenith angle smaller than 70 °, near-nadir and cloud-free pixels.

#### 3.1 Solar irradiance

Using the satellite measured solar irradiance for the DOAS SO<sub>2</sub> retrieval can effectively reduce instrument-related errors. However, due to the degradation and non-uniformity of the diffuser plate of OMS, the OMS L1 irradiance measurements experienced increasing errors after launch, especially in the shortwave UV region (for more information see section 5.1). Therefore, in this study the TSIS HSRS hybrid solar reference spectrum (Coddington et al., 2021) was used for OMS SO<sub>2</sub> retrievals instead of OMS daily measured solar irradiance. The TSIS HSRS hybrid solar reference spectrum was developed by normalizing high spectral resolution solar datasets to the absolute irradiance scale of the TSIS-1 Spectral Irradiance Monitor (SIM) and the CubeSat Compact SIM (CSIM). The high spectral resolution solar data are sourced from the Air Force Geophysical Laboratory (AFGL) ultraviolet solar irradiance balloon observations, the ground-based Quality Assurance of Spectral Ultraviolet Measurements in Europe Fourier Transform Spectrometer (QASUMEFTS) solar irradiance observations, the Kitt Peak National Observatory (KPNO) solar transmittance atlas, and the semi-empirical Solar Pseudo Transmittance Spectrum (SPTS) atlas. The TSIS-1 HSRS spans 202–2730 nm at 0.01 to ~0.001 nm spectral resolution with uncertainties of 0.3% between 460 and 2365 nm and 1.3% at wavelengths outside that range (Coddington et al., 2021). The TSIS HSRS hybrid solar reference spectrum was convolved with the OMS-N ISRF to match the spectral characteristics of OMS radiance. The FY3F/OMS-N ISRF was determined using tunable laser scanning with a step size of 0.02 nm,



providing the relative response of each detector pixel on the focal plane arrays to monochromatic illumination (Wang et al., 2024). It varies in both the spectral and spatial dimensions of the two large array detectors. The shape of the FY3F/OMS-N ISRF exhibits a flat top in the central peaks because OMS-N adopts a stereoscopic slit observation mode. The TSIS HSRS hybrid solar reference spectrum provides high accuracy solar irradiances, but as it was not measured with the OMS-N instrument, any calibration issues in the radiances do not cancel in the DOAS retrieval. Therefore, its use may lead to systematic overestimation or underestimation in the retrieved SO<sub>2</sub> columns, as well as along-track stripes, which cannot be fully corrected through post-processing algorithms.

### 3.2 Spectral soft calibration

Before the DOAS fitting retrieval, spectral soft calibration was applied to the FY3F/OMS radiance data. Spectral soft calibration can correct wavelength shifts caused by factors such as instrument drift, temperature fluctuations, radiation effects, and nonlinear effects, using known absorption features to adjust the initial L1 data. The spectral soft calibration process ensures the accuracy and consistency of the OMS radiances, which is essential for accurate SO<sub>2</sub> retrieval and for minimizing the impact of calibration errors on the SO<sub>2</sub> retrieval.

The spectral soft calibration is performed using the peaks and valleys of the TSIS HSRS hybrid solar reference spectrum (Van Geffen and Van Oss, 2003; Coddington et al., 2021). The detailed process includes: 1) Selecting the high-resolution hybrid solar reference spectrum (Coddington et al., 2021), and convolving the reference spectrum with the slit function of the FY3F/OMS instrument; 2) Fitting the ratio of the solar reference spectrum to the observed radiance spectrum with a low-order polynomial to enhance the observed radiance spectrum; 3) For each observed radiance spectrum in the SO<sub>2</sub> fitting window, Gaussian peak-finding is performed to match the peak position of a set of Fraunhofer lines with their corresponding wavelengths. A least-squares method is used to fit the spectral line wavelengths and the peak position number data with a third-order polynomial, generating a spectral calibration equation for each observed pixel. Then the spectral soft calibration of the FY3F/OMS radiance was realized by using the above spectral calibration equation.

### 3.3 DOAS SCD retrieval

#### 3.3.1 SO<sub>2</sub> fitting window

The selection of the retrieval fitting window is crucial for the accuracy of OMS SO<sub>2</sub> retrievals, which significantly affect OMS capability in monitoring SO<sub>2</sub> from volcanic and anthropogenic sources. A suitable fitting window helps to reduce the impact of interfering gases (O<sub>3</sub>), to enhance the SO<sub>2</sub> information content in the satellite signal and to obtain reliable SO<sub>2</sub> results. In this study, the 312-326 nm fitting window is chosen for the SO<sub>2</sub> retrieval from OMS observations. This is mainly based on the following considerations:

(1) Firstly, in the wavelength range 310-330 nm, although SO<sub>2</sub> has stronger absorption at shorter wavelengths (Fig. 1) which would make it preferable, satellite measurements at shorter wavelengths have lower SNR, and in the case of volcanic SO<sub>2</sub>



emission, the TOA reflected radiances are prone to saturation which leads to underestimation of volcanic SO<sub>2</sub>. Therefore, it is not appropriate to select the fitting window with the strongest SO<sub>2</sub> absorption for SO<sub>2</sub> retrieval.

145 (2) Secondly, longer UV wavelengths, due to the weaker absorption of SO<sub>2</sub>, tend to introduce more noise into the retrieval of the SO<sub>2</sub> column. This is because the weaker absorption may make it more difficult to accurately distinguish the SO<sub>2</sub> absorption information from background noise and interference of O<sub>3</sub> absorption, especially in the case of low SO<sub>2</sub> emissions from anthropogenic sources.

(3) Thirdly, selecting the 312–326 nm fitting window makes the OMS SO<sub>2</sub> product consistent with the widely used  
150 TROPOMI SO<sub>2</sub> product (Theys et al., 2017). However, in this study, we did not adopt a strategy with multiple fitting windows for different SO<sub>2</sub> concentration conditions as is used in the TROPOMI product.

(4) Finally, in order to demonstrate the advantage of the 312–326 nm fitting window for OMS SO<sub>2</sub> retrievals, comparisons were conducted between SO<sub>2</sub> retrievals from different fitting windows over the Sundhn̄kur volcano and its surrounding clean region for August 23, 2024 (Figs. 2, 3, and 4). Note that negative values often appear in SO<sub>2</sub> retrievals, and small  
155 negative values can indicate low SO<sub>2</sub> emissions in clean areas. In this study, all SO<sub>2</sub> retrievals greater than -10 DU are selected for comparison to exclude obvious outliers. The details of the comparisons are described below.

The main fitting windows and retrieval algorithms used in the literature for SO<sub>2</sub> retrievals based on ultraviolet hyperspectral satellite measurements are listed in Table 2. The OMS SO<sub>2</sub> columns retrieved using these different fitting windows are shown in Figs. 2, 3, and 4. Note that due to the DOAS algorithm generally using a continuous UV fitting window for SO<sub>2</sub>  
160 retrieval, the OMS SO<sub>2</sub> results from BRD four discrete wavelengths (310.8, 311.9, 313.2, and 314.4 nm) at absorption peak and valley (Krotkov et al., 2006) are not included in this study. It also should be noted that, since the OMS VIS spectral band starts from 307 nm and the OMS UV2 spectral range from 300 nm to 320 nm requires further calibration, the 300–335 nm fitting window used by the EISF algorithm was not tested in this section.

As shown in Figs. 2 and 3, the retrieval results of SO<sub>2</sub> columns from the 315–327 nm, 325–335 nm, 360–390 nm, 317.8–333  
165 nm, and 315–326 nm fitting windows are first excluded due to the large errors observed in the clean regions (e.g., OMS cross-track positions 1–150). The retrieval results from the 308–333 nm fitting window are also excluded because the results are relatively lower in the volcanic region than those from the other fitting windows. Finally, according to the retrieval results of SO<sub>2</sub> columns in Fig. 4, the retrieval results from the 312–326 nm and 312–330 nm fitting windows show higher and similar values in the volcanic region. Additionally, in the clean regions (cross-track positions 1–150), both 312–326 nm  
170 and 312–330 nm fitting windows exhibit lower and similar standard deviations and mean values. Therefore, considering all the above reasons and to be consistent with the TROPOMI DOAS SO<sub>2</sub> product, the 312–326 nm fitting window was selected for OMS SO<sub>2</sub> retrieval in this study.

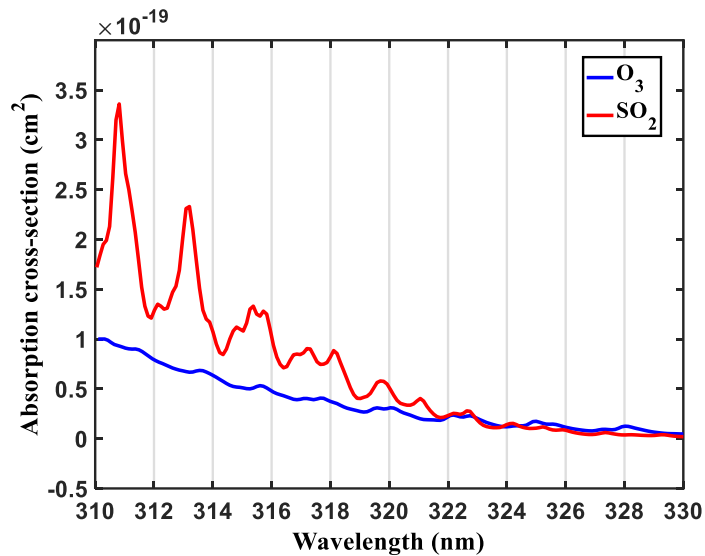


Figure 1: Absorption cross sections of SO<sub>2</sub> and O<sub>3</sub> in the wavelength range 310–330 nm (Bogumil et al., 2003).

175

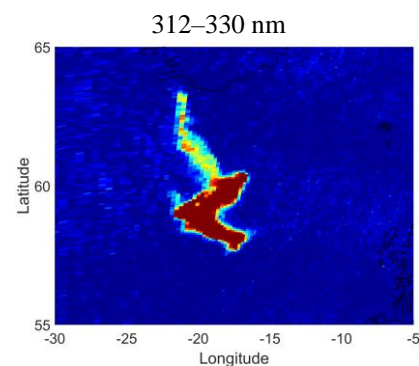
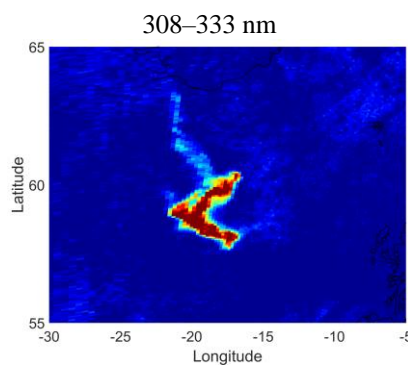
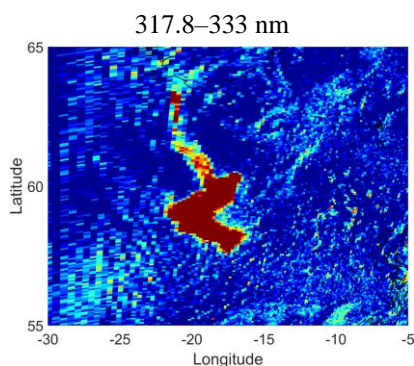
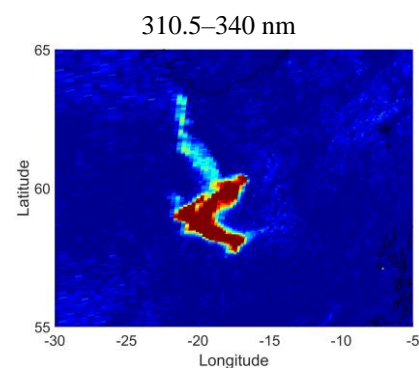
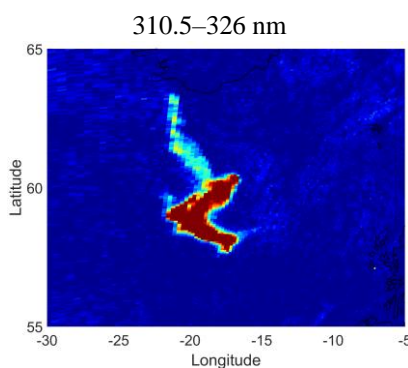
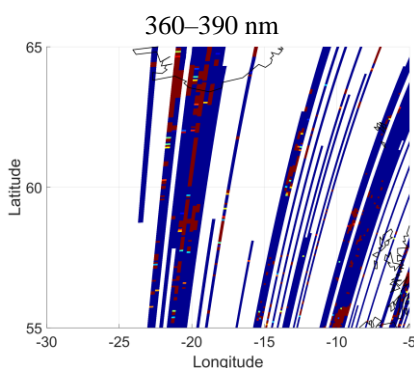
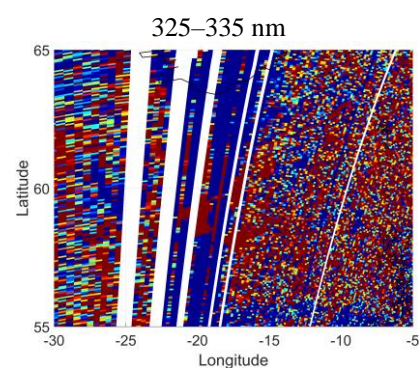
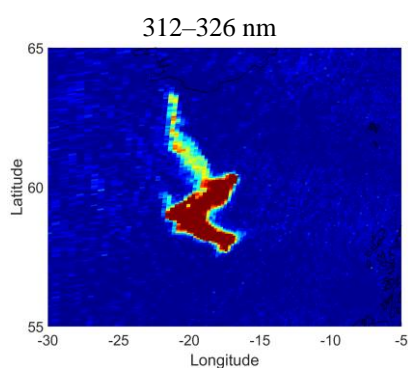
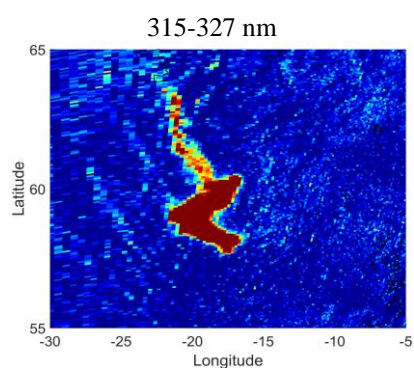
Table 2. Retrieval algorithms and fitting windows used for SO<sub>2</sub> retrieval from UV-VIS hyperspectral satellite measurements

Instruments	Retrieval algorithms	Fitting windows
SCIAMACHY	DOAS	315–327 nm (Platt and Stutz, 2008; Richter et al., 2006)
OMI	Principal Component Analysis (PCA)	310.5–340 nm (Li et al., 2013)
	Iterative Spectral Fitting (ISF)	317.8–333 nm (Yang et al., 2009)
	Extended Iterative Spectral Fitting (EISF)	300–335 nm (Yang et al., 2010)
	Band Residual Difference (BRD)	Four discrete wavelengths (310.8, 311.9, 313.2, and 314.4 nm) (Krotkov et al., 2006)
GOME-2	Optimal Estimation (OE)	312–330 nm (Nowlan et al., 2011)
	DOAS	315–326 nm (Fioletov et al., 2013)
OMPS	Iterative Spectral Fitting (ISF)	308–333 nm (Yang et al., 2013)

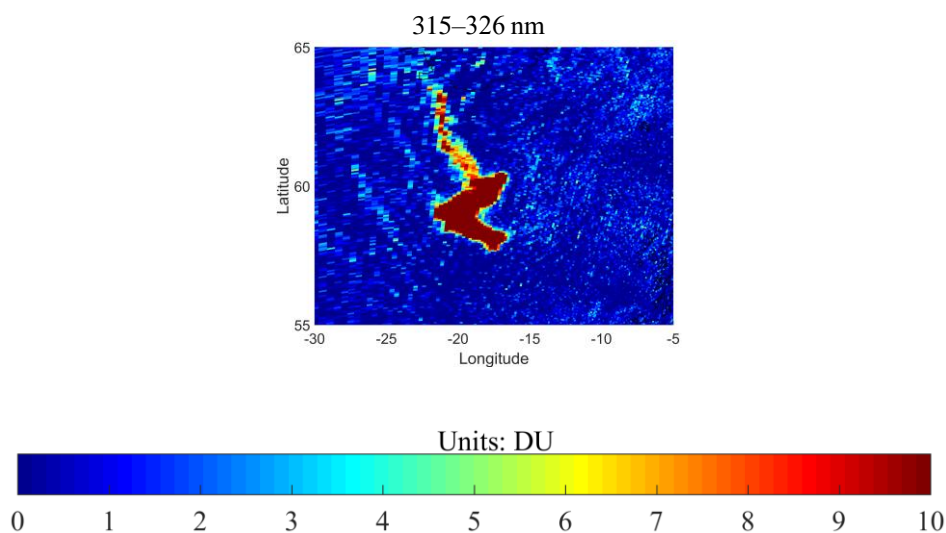




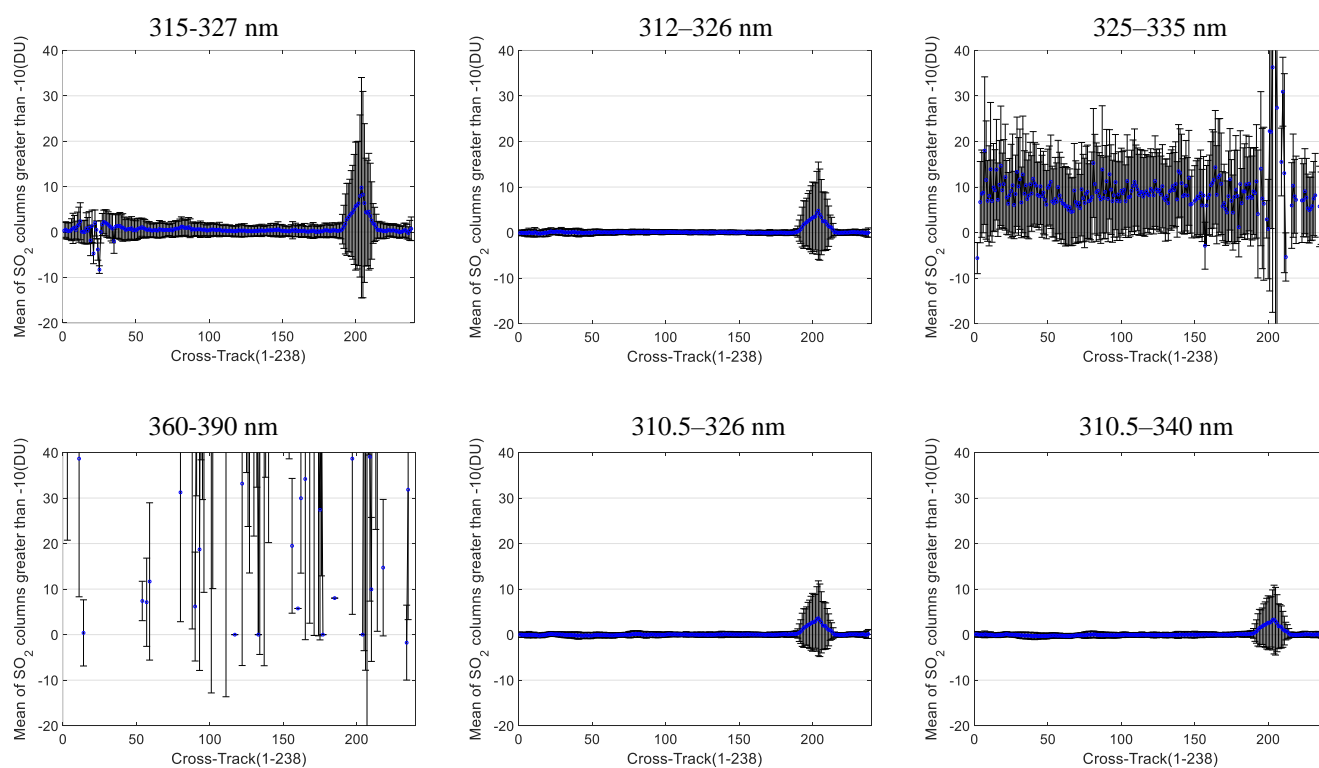
TROPOMI	DOAS	312–326 nm, 325–335 nm, and 360–390 nm (Theys et al., 2017)
	COBRA	310.5–326 nm (Theys et al., 2021)







**Figure 2: SO<sub>2</sub> retrievals from different fitting windows over the Sundhnúkur volcano on August 23, 2024 (OMS orbit 20240823\_1036). DU=Dobson Units, 1DU=2.69×10<sup>16</sup> molecules/cm<sup>2</sup>. The missing pixels in the figures are caused by inversion failures resulting in Nan values.**



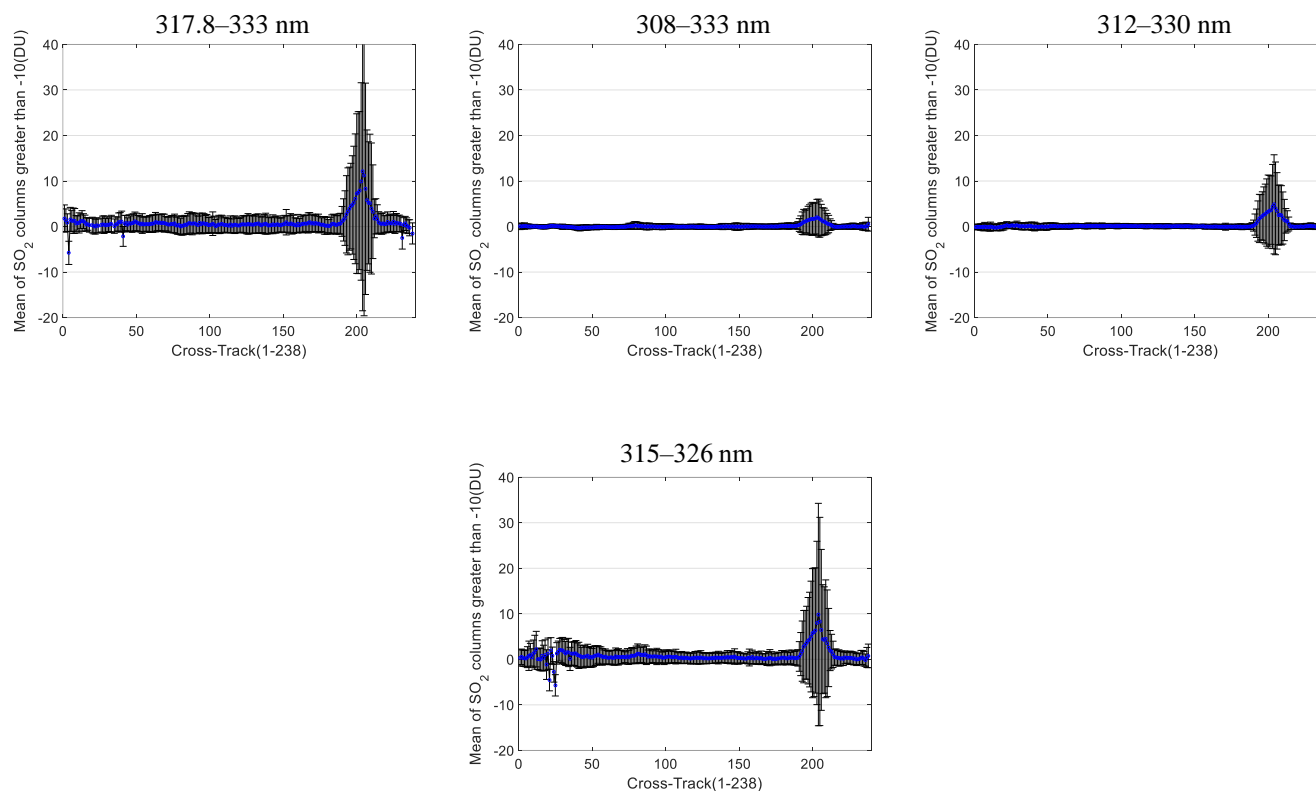


**Figure 3: Variation and standard deviations of row-averaged SO<sub>2</sub> retrievals from different fitting windows at Cross-Track positions over Sundhnúkur volcano and its surrounding region on August 23, 2024, OMS rows from 700 to 870 of orbit 20240823\_1036.**

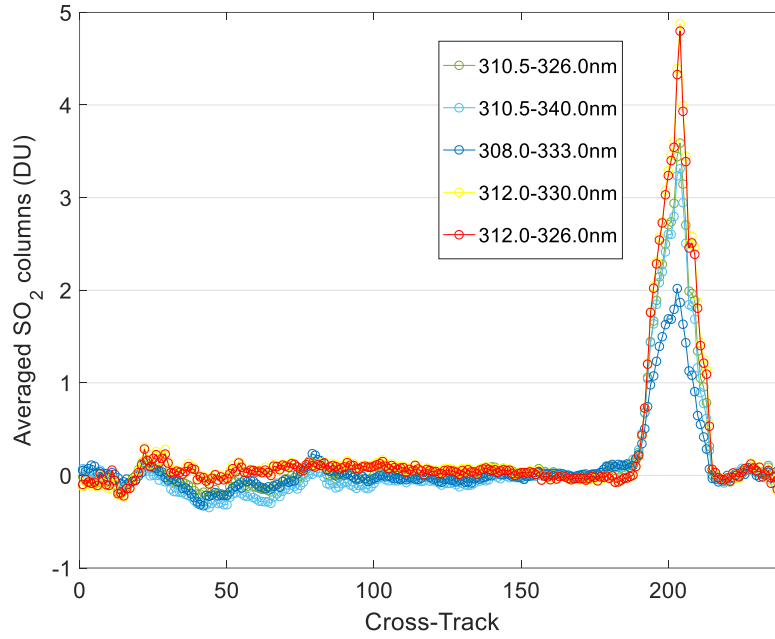


**Figure 4: Row-averaged SO<sub>2</sub> retrievals from OMS rows 700 to 870 of orbit 20240823\_1036 by using different spectral fitting windows. For Cross-Track positions 1–150, the standard deviations and mean values of SO<sub>2</sub> retrievals are 0.08 DU and 0.04 DU for the 312–326 nm window, 0.09 DU and -0.03 DU for 310.5–326 nm, 0.10 DU and -0.10 DU for 310.5–340 nm, 0.09 DU and -0.04 DU for 308–333 nm, and 0.09 DU and 0.06 DU for 312–330 nm, respectively.**

### 3.3.2 The Ring effect

The Ring effect refers to the phenomenon that the Fraunhofer lines present in the solar spectrum from absorption in the solar atmosphere by elements such as potassium and calcium are partially filled in spectra of scattered light taken in the Earth's atmosphere (Grainger and Ring, 1962). For the Ring effect in satellite-observed spectra, the primary source is the rotational Raman scattering of N<sub>2</sub> and O<sub>2</sub> molecules in the atmosphere, which redistributes photon energy and leads to the filling-in of Fraunhofer and atmospheric absorption lines (Sioris and Evans, 1999; Fish and Jones, 1995; Chance and Spurr, 1997; Vountas et al., 1998). For OMS SO<sub>2</sub> column retrievals using the DOAS method, the Ring effect is an important factor influencing the accuracy of retrieval results due to the strong Ring spectrum in the UV wavelength band (Fig. 5). Taking the OMS 20240823\_1036 orbit as an example, after including the Ring spectrum into the DOAS retrieval, the spectral fitting residual RMSE for most OMS pixels decreases by approximately 0.004 to 0.01.

In this study, during the OMS SO<sub>2</sub> DOAS retrieval, the Ring effect is considered as a pseudo-absorption effect, and the Ring spectrum calculated using the SCIATRAN radiative transfer model (Rozanov et al., 2005) is included as a pseudo-absorber in the spectral fitting process, as shown in Equation (1).

$$-\ln \frac{\pi \cdot I(\lambda)}{F(\lambda) \cdot \cos(SZA)} = \sigma_{\text{SO}_2}(\lambda) \times \text{SCD}_{\text{SO}_2} + \sigma_{\text{O}_3}(\lambda) \times \text{SCD}_{\text{O}_3} + \sigma_{\text{Ring}}(\lambda) \times C_{\text{Ring}} + P(\lambda) + E(\lambda) \quad (\text{Eq. 1})$$



Where  $I(\lambda)$  and  $F(\lambda)$  are the satellite-observed radiance and the solar reference spectrum convolved with the OMS ISRF,  $SCD_{SO_2}(\lambda)$  and  $SCD_{O_3}(\lambda)$  are the absorption cross-section of  $SO_2$  and  $O_3$ ,  $SCD_{SO_2}$  and  $SCD_{O_3}$  are the slant column density of  $SO_2$  and  $O_3$ ,  $\sigma_{Ring}(\lambda)$  is the Ring spectrum calculated using the SCIATRAN model and convolved with the OMS ISRF,  $C_{Ring}$  is the Ring absorption coefficient determined by the fitting,  $P(\lambda)$  is a low-order polynomial, and  $E(\lambda)$  is the error term. Note that in this study the SCIATRAN Ring spectrum for typical atmospheric conditions and observational geometry ( $SCA=30^\circ$ , Viewing Zenith Angle ( $VZA$ )= $0^\circ$ , Relative Azimuth Angle ( $RAA$ )= $0^\circ$ , surface reflectance ( $AS$ )=0.05, surface height above sea level ( $HS$ ) (also referred to as terrain height)=0 km, ozone column=275 DU, clear sky) is used in the DOAS fitting for all OMS measurements, without considering the variations of the Ring spectrum due to different atmospheric conditions and viewing geometries.

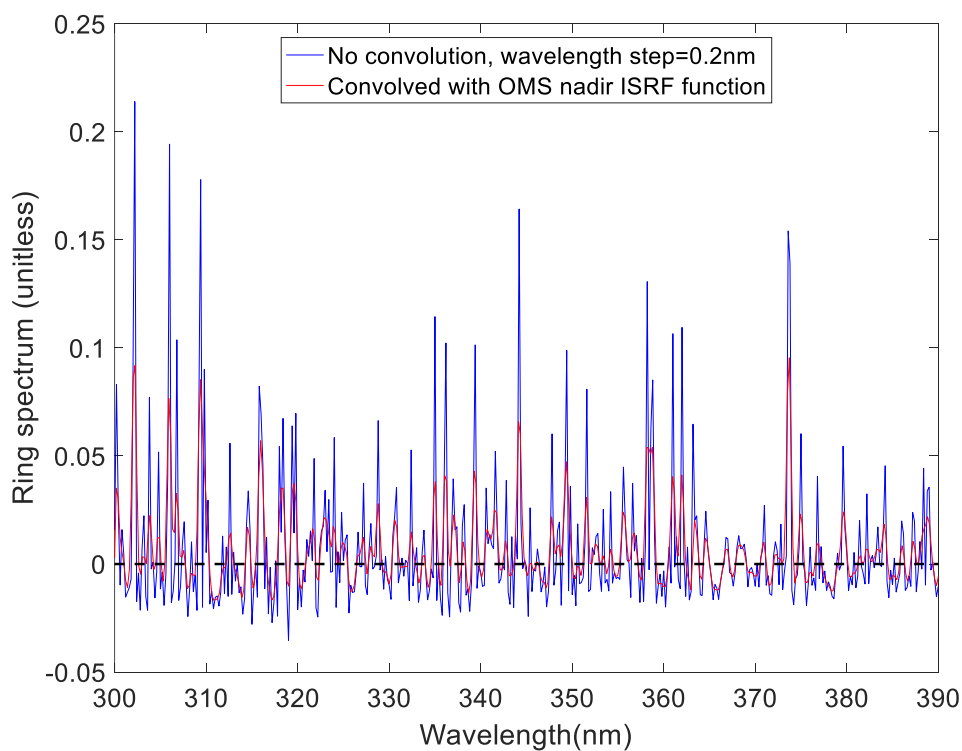


**Figure 5: Ring spectrum calculated with the SCIATRAN model, convolved with the OMS ISRF. SCIATRAN forward settings are  $SCA=30^\circ$ ,  $VZA=0^\circ$ ,  $RAA=0^\circ$ , Surface albedo=0.05, Ozone column=275 DU, Clear sky.**

### 3.3.3 Spectral fitting

The retrieval of the FY3F/OMS  $SO_2$  SCD is primarily based on the classical DOAS theory (Platt and Stutz, 2008). It utilizes Beer-Lambert's law and the satellite hyperspectral radiance observations in the UV fitting window to derive the  $SO_2$  SCD along the entire photon path. First, the absorption cross-section of  $SO_2$  and  $O_3$ , measured under specific laboratory conditions



with a higher spectral resolution and different sampling points than those of OMS observations, are convolved with the OMS ISRF to match the spectral resolution of the OMS instrument. Secondly, atmospheric extinction is divided into two components: a fast-varying part with wavelength, typically associated with narrow absorption features of SO<sub>2</sub> and O<sub>3</sub>, and a slow-varying part with wavelength, related to broad spectral features of absorption and atmospheric scattering processes such as Rayleigh and Mie scattering. A low-order polynomial is used to remove the slow-varying components, while preserving the fast-varying part related to SO<sub>2</sub> and O<sub>3</sub> absorption. Finally, the slow-varying part of satellite-observed TOA reflectance (the ratio of L1 radiance to irradiance data) are removed by subtracting a low-order polynomial, and the atmospheric SO<sub>2</sub> SCD is obtained through least-squares fitting.

**Table 3. Parameter settings for the retrieval of FY3F/OMS SO<sub>2</sub> SCD**

Parameter	FY3F/OMS SO <sub>2</sub> DOAS settings
Retrieval fitting window	312–326 nm
Solar irradiance	TSIS HSRS hybrid solar reference spectrum (Coddington et al., 2021)
Cross-sections	SO <sub>2</sub> 273K (Bogumil et al., 2003) O <sub>3</sub> 223K (Bogumil et al., 2003)
Ring effect	Ring spectrum calculated using the SCIATRAN model at SZ A=30 °, VZA=0 °, RAA=0 °, AS=0.05, Clear sky (Rozanov et al., 2005)
Polynomial	3 <sup>th</sup> order
Background offset correction	Iterative and sliding correction scheme

**3.4 Background offset correction**

The retrieval accuracy of SO<sub>2</sub> columns from satellite measurements is usually affected by spectral and radiometric calibration errors, which are difficult to remove from L1 radiance data and result in systematic biases in the retrieval results, such as along-track stripes and cross-track asymmetry (Boersma et al., 2004). In addition, due to the low SNR of measurements in the fitting window, the weak SO<sub>2</sub> absorption information included in the TOA reflected radiance, and the interference from strong O<sub>3</sub> absorption in the fitting window, the OMS SO<sub>2</sub> retrievals tend to be systematically overestimated or underestimated over the whole orbit. These systematic biases in the retrieval results of SO<sub>2</sub> columns are mixed with the



absorption information of SO<sub>2</sub> and limit the applicability of the OMS SO<sub>2</sub> product. Therefore, it is necessary to apply a background offset correction to reduce these systematic biases in the retrieved SO<sub>2</sub> columns. The reference region method (Khokhar et al., 2005; Richter et al., 2006) was used to correct the background offsets, which are latitude-dependent and related to the cross-track position. This method selects retrieval values over a reference region (e.g., clean oceanic Pacific regions, assumed to be areas with no SO<sub>2</sub>) as the background area. The SO<sub>2</sub> retrievals are then adjusted by subtracting the background offsets of the same latitude over the ocean. Yang proposed the sliding median correction method (Yang et al., 2007) and applied it to the OMI SO<sub>2</sub> product. This method performs averaged sampling within a sliding window centered on the pixel (selecting pixels with values less than 2 DU) to get background offsets for each row of pixels. With the sliding window method, the cross-track and along-track biases varying with time and location can be effectively eliminated.

For OMS SO<sub>2</sub> retrievals, based on the above background offset correction methods, we developed an improved iterative sliding correction scheme to avoid seam problems due to discontinuous integration times within the same orbit. The details of the background offset correction used for OMS SO<sub>2</sub> retrievals are as follows.

(1) Firstly, based on the integration time of FY3F/OMS L1 data, the orbital data is divided into several data blocks corresponding to different integration times. For each data block, the mean vector (V0) at each cross-track position is estimated using all valid pixels within the block (i.e., pixels with normal L1 data, as indicated by the L1 QA quality flag). Each scan line within the data block is processed by subtracting V0 from the SO<sub>2</sub> retrievals of each scan line to obtain the initially corrected SO<sub>2</sub> columns.

(2) Secondly, based on the initially corrected SO<sub>2</sub> columns, the predefined SO<sub>2</sub> threshold (2 DU), and the sliding window, the mean vector V1 for cross-track positions within each sliding window is estimated. The initially corrected SO<sub>2</sub> columns are then processed by subtracting V1 to obtain the double-corrected SO<sub>2</sub> columns. Note that the size of the sliding window varies with the satellite's spatial resolution. In this study, for the FY3F/OMS with nadir resolution of 7 km×7 km, the sliding window is set to 200 scan lines. It is worth noting that there is a trade-off between the size of the sliding window and the effectiveness of the offset correction: too big a window might result in poor offset correction, while too small a sliding window might lead to reduction of the SO<sub>2</sub> information contained in the satellite measurements.

(3) Finally, based on the double-corrected SO<sub>2</sub> results, the predefined SO<sub>2</sub> threshold, and the sliding window, an iterative procedure is performed until the relative deviation between the results of the two consecutive corrections is less than or equal to 5%.

### 3.5 AMF

The reflected radiance detected by the satellite instrument contains information of trace gases integrated along the slant observation path. From the reflected radiance and above DOAS spectral fitting, the SO<sub>2</sub> SCD can be derived; however, the SCD is not suitable for the application of satellite-derived SO<sub>2</sub> in monitoring global climate change and air pollution, as it represents the SO<sub>2</sub> column along the slant path, which is influenced by the observation geometry and atmospheric conditions.





265 The SCD can be converted to VCD using  $AMF = SCD/VCD$  (Palmer et al., 2001), which represents the relative length of the mean slant path at a certain wavelength for photons interacting with a certain absorber in the atmosphere relative to the vertical path (Lorente et al., 2017). The AMF can be calculated by using Box-AMF from forward radiative transfer model and local  $SO_2$  profile (Chen et al., 2009; Wagner et al., 2007; Palmer et al., 2001; Boersma et al., 2004). However, due to the difficulty in obtaining accurate and satellite-synchronized global  $SO_2$  profiles, we adopted a simplified approach that uses  
270 two constant AMF values representative for typical conditions for the OMS  $SO_2$  conversion from SCD to VCD in this study. One is  $AMF=1$  for clean regions and non-ice/snow-covered areas influenced by anthropogenic sources and volcanic eruptions, while the other is  $AMF=2$  for the ice/snow-covered areas. These two AMF constants are approximate values derived using the SCIATRAN Box-AMF and a 5 DU anthropogenic  $SO_2$  profile under typical atmospheric and surface conditions ( $SZA = 32.9^\circ$ ,  $VZA = 0^\circ$ ,  $RAA = 0^\circ$ ,  $AS = 0.05$ ,  $HS = 0$  km, wavelength = 320 nm, a 365 DU midlatitude ozone  
275 profile (Sinnhuber et al., 2009), and with the assumption of surface reflectance as isotropic Lambertian equivalent reflector (LER)). Section 5.2 of this study provides a more detailed description of Box-AMF and an error analysis of the AMF.

#### 4 Comparison of OMS $SO_2$ columns with TROPOMI observations

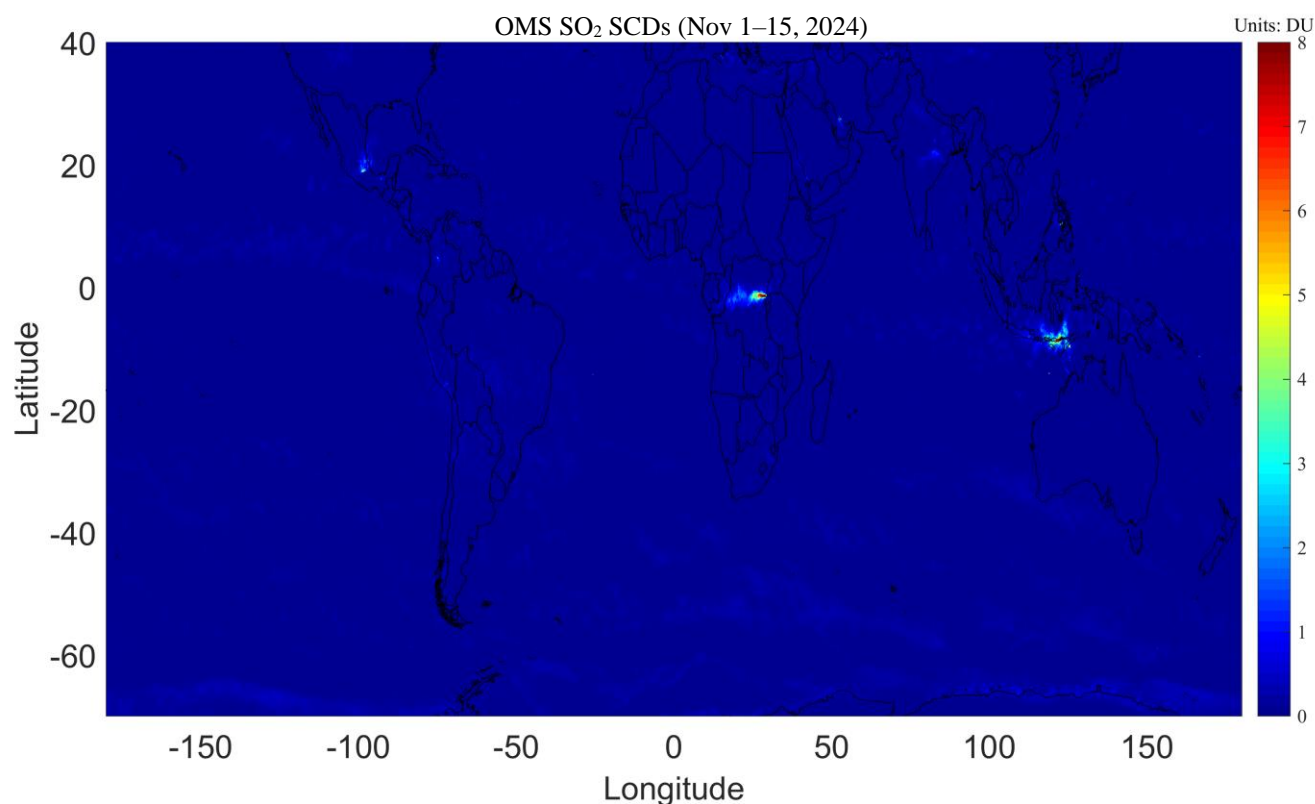
Based on the FY3F/OMS L1 measurements and the retrieval scheme outlined in section 3, global  $SO_2$  columns from FY3F/OMS were retrieved and applied to monitor the  $SO_2$  emissions from volcanic and anthropogenic activities. Evaluating  
280 the accuracy of OMS  $SO_2$  retrievals is challenging, as it is difficult to obtain synchronous and high-quality ground-based or airborne measurements for the validation of OMS  $SO_2$  retrievals. Therefore, in this study, due to its high spatial and spectral resolution in the UV-VIS band and its common use in global  $SO_2$  monitoring, the TROPOMI  $SO_2$  total column product was selected as reference to evaluate the accuracy of OMS  $SO_2$  retrievals (Theys et al., 2019; Wang et al., 2022; Theys et al., 2017; Cofano et al., 2021; Corradino et al., 2024; Fioletov et al., 2020).

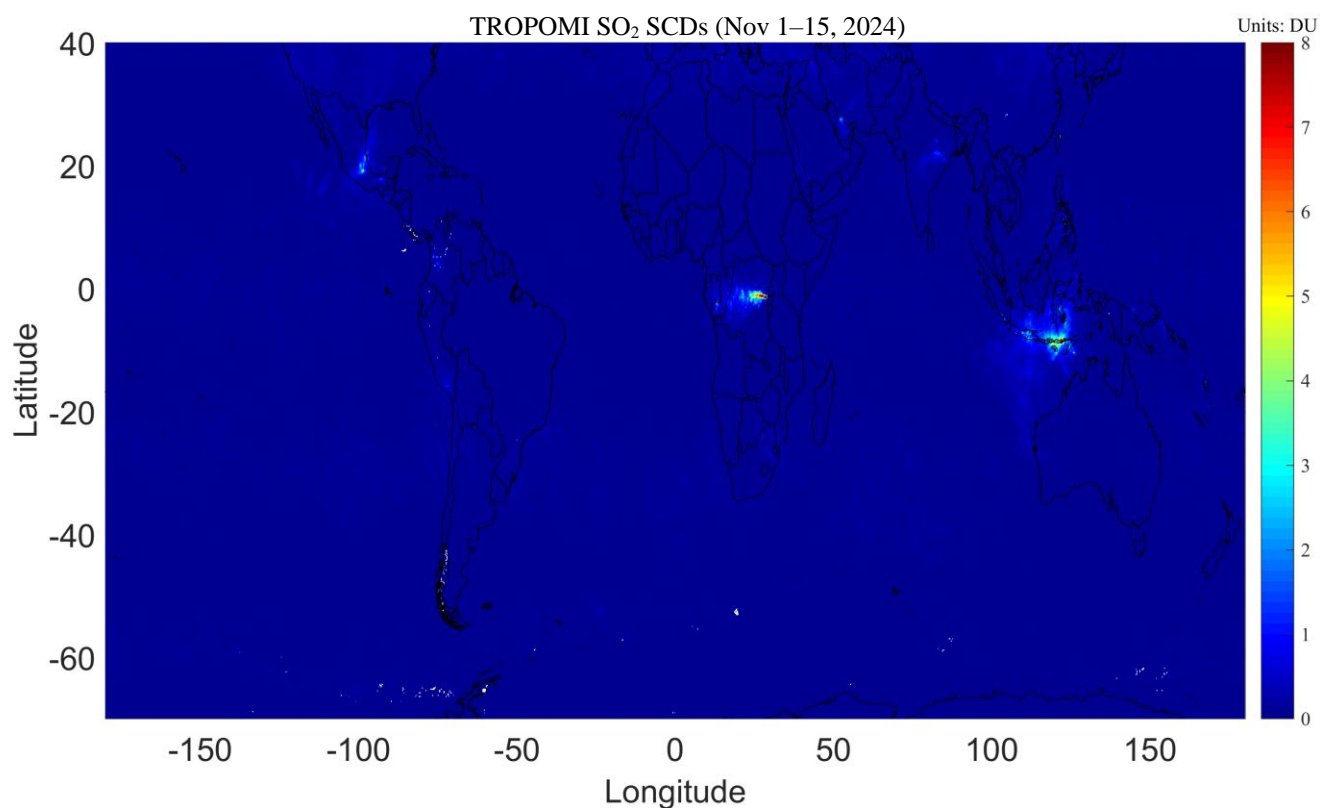
285 TROPOMI has a local overpass time of 13:30, a spatial resolution of 5.5 km $\times$ 3.5 km for  $SO_2$  and provides daily global coverage with  $\sim 14$  orbits per day. TROPOMI  $SO_2$  products from two algorithms are used for comparison: one is the TROPOMI offline L2 orbital  $SO_2$  product from the DOAS algorithm (hereafter referred to as TROPOMI DOAS) (Data source: <https://browser.dataspace.copernicus.eu/>), and the other is the TROPOMI L3 grid Planetary Boundary Layer (PBL) and 7km  $SO_2$  product from the COBRA algorithm (hereafter referred to as TROPOMI COBRA) (Data source: <https://data-portal.s5p-pal.com/products/SO2cbr.html>). The TROPOMI COBRA  $SO_2$  product was developed by Royal Belgian Institute for Space Aeronomy (BIRA), and reduces significantly both the noise and biases present in the current TROPOMI operational DOAS  $SO_2$  retrievals (Theys et al., 2021). The TROPOMI COBRA L3 grid product ( $0.022^\circ \times 0.022^\circ$  equal latitude-longitude grid) was generated using the HARP gridding tool from L2 data applying a Quality Assurance (QA) filter ( $QA > 0.5$ ) to remove low quality data.

290 Figure 6 shows the 15-days averaged global  $SO_2$  SCDs from OMS DOAS and TROPOMI DOAS from November 1st to 15th, 2024. The OMS DOAS  $SO_2$  SCDs were averaged using pixels with  $SO_2$  column greater than -10 DU, whereas the



TROPOMI DOAS SO<sub>2</sub> SCDs were averaged using pixels with QA > 0.5. It is worth noting that since negative values often appear in SO<sub>2</sub> retrievals, and small negative values can indicate low SO<sub>2</sub> emissions in clean areas, in this study OMS SO<sub>2</sub> retrievals greater than -10 DU are selected for comparison. As shown in Fig. 6, the OMS and TROPOMI DOAS SO<sub>2</sub> SCDs exhibit generally consistent spatial distributions, both clearly identifying the major global SO<sub>2</sub> emission hotspots. However, there are slight differences between the OMS and TROPOMI DOAS SO<sub>2</sub> SCDs, which may be attributed to differences in observational geometry, overpass time, and algorithmic processing. Further comparisons between OMS, TROPOMI DOAS and TROPOMI COBRA SO<sub>2</sub> columns based on individual orbits are discussed in Sections 4.1, 4.2, and 4.3. The effectiveness of OMS SO<sub>2</sub> retrievals was evaluated by comparing them with TROPOMI over clean oceanic regions, volcanic eruption regions, and anthropogenic emission regions as shown in Fig. 7.





310 **Figure 6: Global maps of averaged SO<sub>2</sub> SCDs from OMS DOAS and TROPOMI DOAS during the period of November 1st to 15th, 2024, 0.2°×0.2° equal latitude-longitude grid. Note that the TROPOMI DOAS SO<sub>2</sub> SCDs are obtained from the product variable ‘fitted\_slant\_columns\_win1’, corresponding to the 312–326 nm wavelength fitting window.**

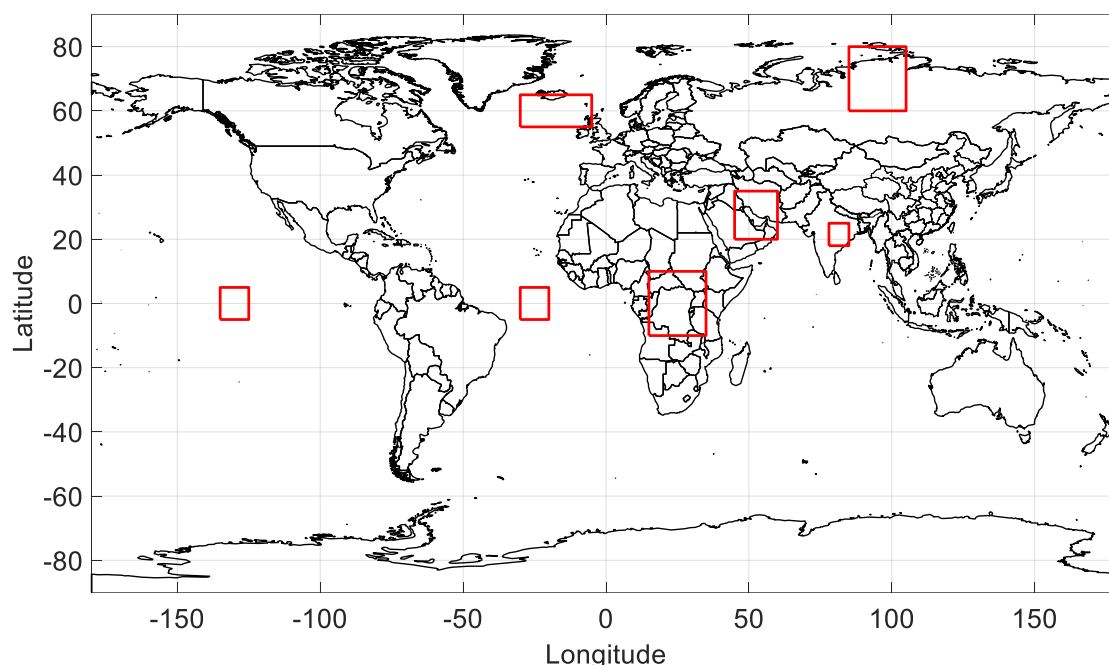


**Figure 7: Regions selected for the comparison of OMS and TROPOMI SO<sub>2</sub> columns.**

#### **4.1 Comparison over clean oceanic regions**

315 Ideally, the retrieved SO<sub>2</sub> values from satellite observations in clean regions should be close to zero. The scatter of SO<sub>2</sub> columns in clean regions can reflect the reliability and stability of the satellite data and the retrieval algorithm (Krotkov et al., 2008). In this study, two clean oceanic regions, where SO<sub>2</sub> emissions are extremely low and assumed to be zero, were selected as the case studies to compare and evaluate the precision of FY3F/OMS SO<sub>2</sub> retrievals. One is the area of latitude from 5°S to 5°N and longitude from 30°W to 20°W (Ocean-Area1), and the other is the area of latitude from 5°S to 5°N and longitude from 135°W to 125°W (Ocean-Area2). Due to the geolocation differences between OMS and TROPOMI orbits, the orbital pixels of OMS and TROPOMI DOAS and TROPOMI COBRA SO<sub>2</sub> product over the two clean oceanic regions were resampled to 0.15°×0.15° equal latitude-longitude grid for comparison. As suggested in the TROPOMI README file, only pixels with QA > 0.5 were used for the TROPOMI DOAS SO<sub>2</sub> product. For the cases of clean oceanic regions, TROPOMI COBRA L3 grid PBL SO<sub>2</sub> products were used instead of the COBRA 7km product. For OMS SO<sub>2</sub> retrievals, all  
325 pixels with SO<sub>2</sub> column greater than -10 DU are selected for comparison.

For Ocean-Area1, both OMS and TROPOMI show low SO<sub>2</sub> values, and the standard deviations of OMS, TROPOMI DOAS and TROPOMI COBRA SO<sub>2</sub> columns over Ocean-Area1 are 0.2117 DU, 0.2468 DU and 0.1156 DU (resampling to 0.15°×0.15° equal latitude-longitude grid) on August 23, 2024, and 0.2154 DU, 0.4134 DU and 0.1865 DU (resampling to 0.15°×0.15° equal latitude-longitude grid) on November 15, 2024, respectively. For Ocean-Area2, the standard deviations of

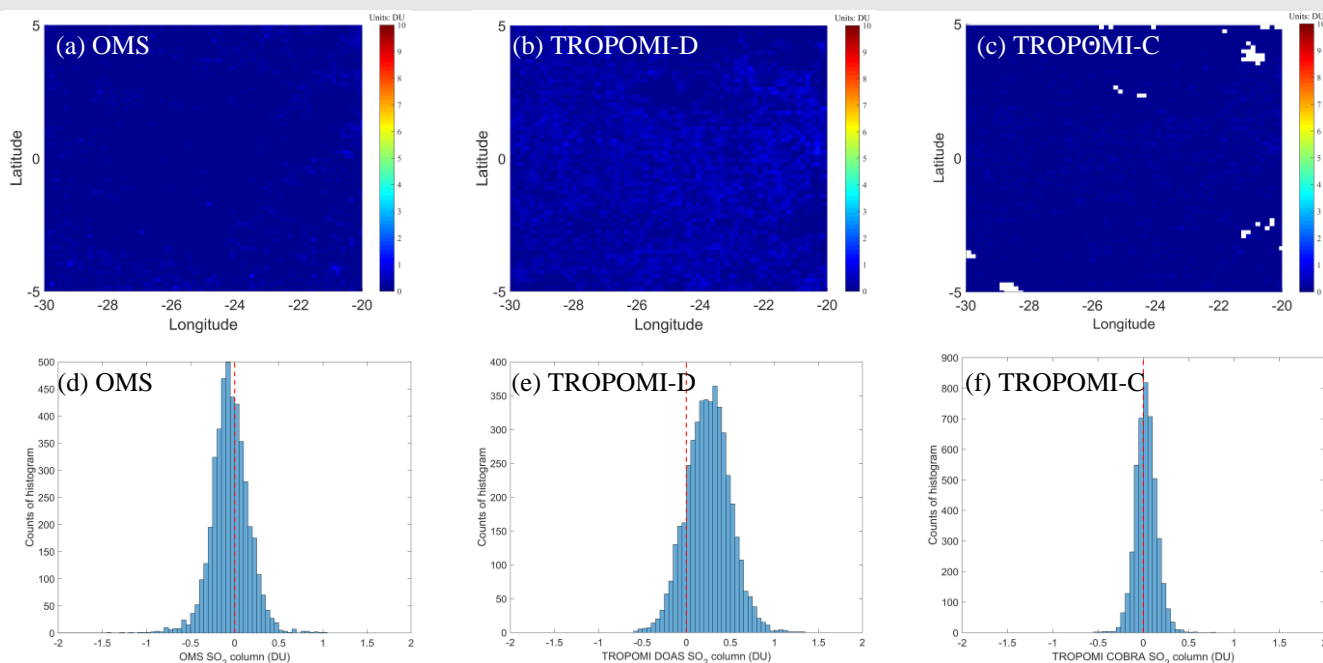


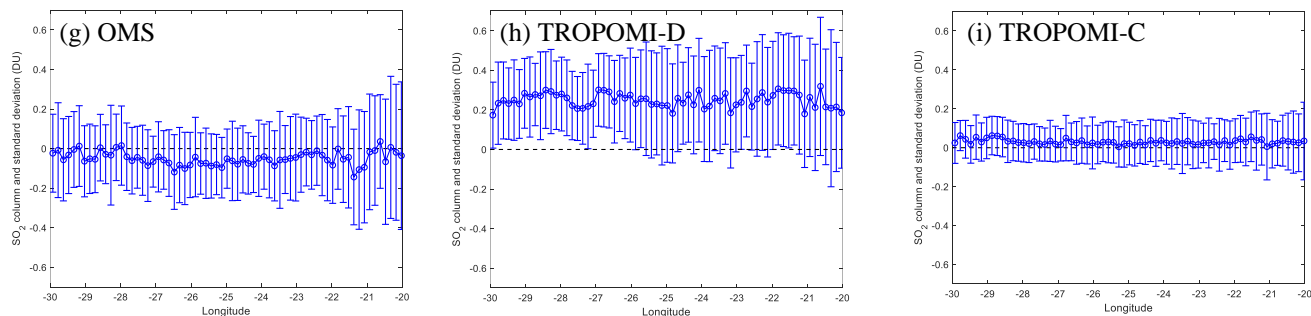
330 OMS, TROPOMI DOAS and TROPOMI COBRA SO<sub>2</sub> columns are 0.2160 DU, 0.2324 DU and 0.1035 DU (resampling to 0.15°×0.15° equal latitude-longitude grid) on August 23, 2024, and 0.2358 DU, 0.3127 DU and 0.1615 DU (resampling to 0.15°×0.15° equal latitude-longitude grid) on November 15, 2024, respectively.

As shown in Figs. 8, 9, 10, and 11, both the SO<sub>2</sub> values of OMS and TROPOMI over Ocean-Area1 and Ocean-Area2 follow approximately a normal distribution centered around 0, with most values concentrated between -2 DU and 2 DU. However, 335 there are small differences between OMS and TROPOMI SO<sub>2</sub> over clean oceanic regions, which become larger as the pixels approach the edge of the orbit. The differences between OMS and TROPOMI SO<sub>2</sub> columns may be related to differences in local overpass time, observation angles, L1 and L2 processing algorithms. Compared with TROPOMI DOAS SO<sub>2</sub> results, TROPOMI COBRA SO<sub>2</sub> results and OMS DOAS SO<sub>2</sub> results have a lower standard deviation and are closer to zero over Ocean-Area1 and Ocean-Area2. The standard deviation of TROPOMI COBRA SO<sub>2</sub> results over the clean oceanic region is 340 lower than that of OMS DOAS SO<sub>2</sub> results, mainly due to the different retrieval schemes and retrieval fitting windows. As shown in Fig. 4, TROPOMI COBRA uses a fitting window of 310.5–326 nm, where the SO<sub>2</sub> absorption is relatively strong, but the signal tends to be saturated under high volcanic SO<sub>2</sub> concentrations.

The comparison results from different dates and different clean oceanic regions show that FY3F/OMS SO<sub>2</sub> retrievals have a reliable precision over low SO<sub>2</sub> emission regions, and the data quality of OMS SO<sub>2</sub> retrievals is relatively stable over time. It 345 is worth noting that the retrieval errors for both OMS and TROPOMI are relatively large at the edges of the orbit. Therefore, the pixels near the edges of the orbit need to be used with caution.

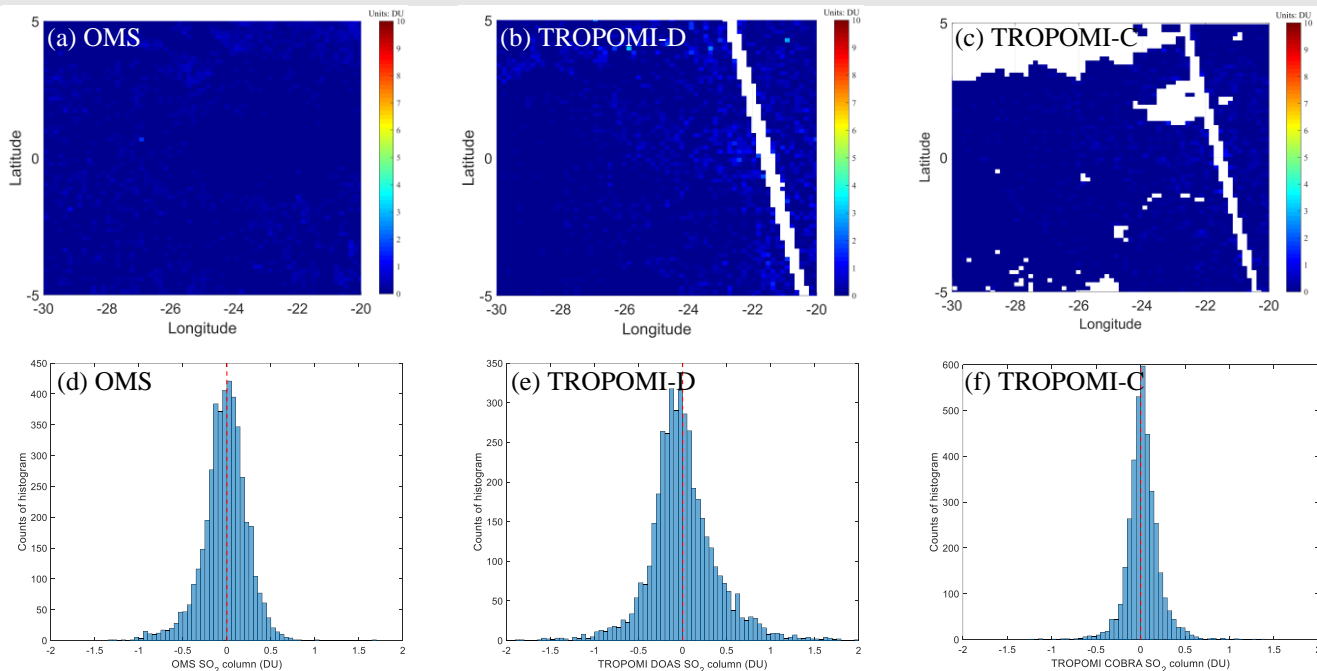
Ocean-Area1, 20240823



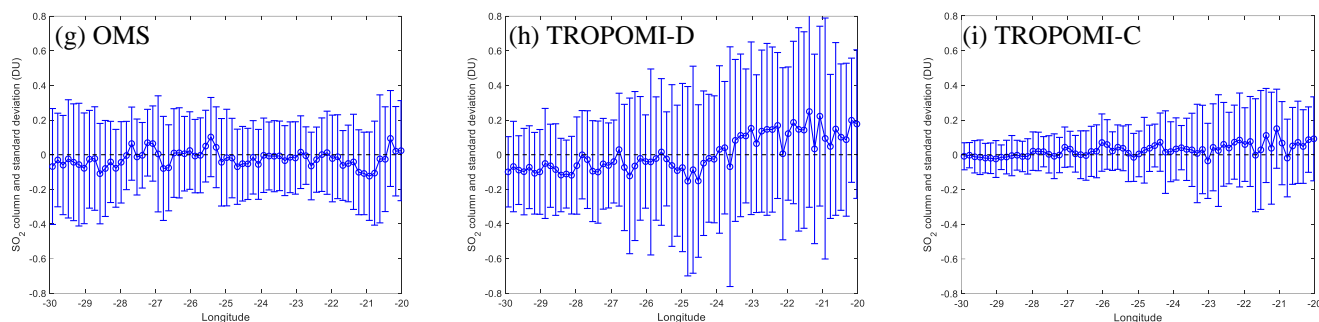


**Figure 8: SO<sub>2</sub> retrievals over clean oceanic area (latitude from 5°S to 5°N and longitude from 30°W to 20°W, Ocean-Area1) on August 23, 2024. (a, b, c) Spatial distribution of resampled FY3F/OMS, TROPOMI DOAS (TROPOMI-D) and TROPOMI COBRA (TROPOMI-C) PBL SO<sub>2</sub> columns over Ocean-Area1; (b, d, f) Histogram of resampled OMS, TROPOMI DOAS and TROPOMI COBRA PBL SO<sub>2</sub> columns over Ocean-Area1; (g, h, i) Variation and standard deviations of the latitude-averaged SO<sub>2</sub> columns over Ocean-Area1. Note that OMS pixels with SO<sub>2</sub> column less than -10 and TROPOMI DOAS pixels with QA < 0.5 are assigned the value of -9999. The missing pixels in the Figure c are caused by Nan values in TROPOMI COBRA data.**

# Ocean-Area1, 20241115



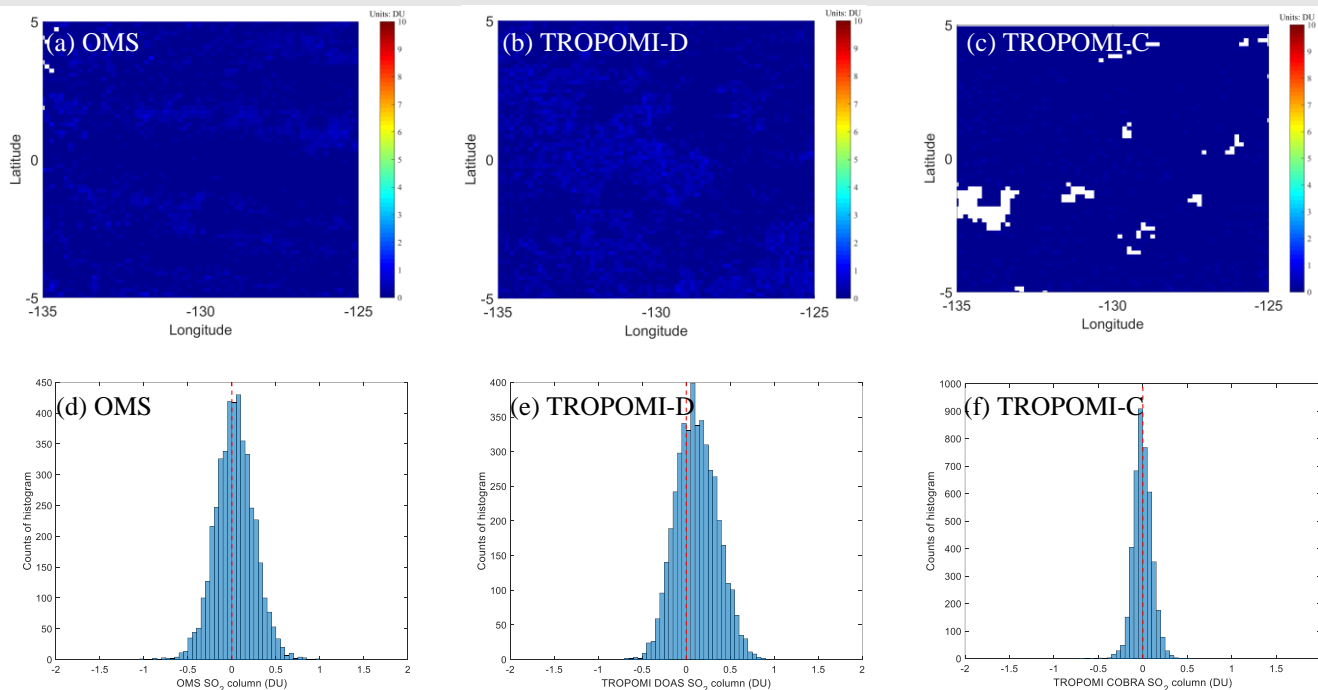


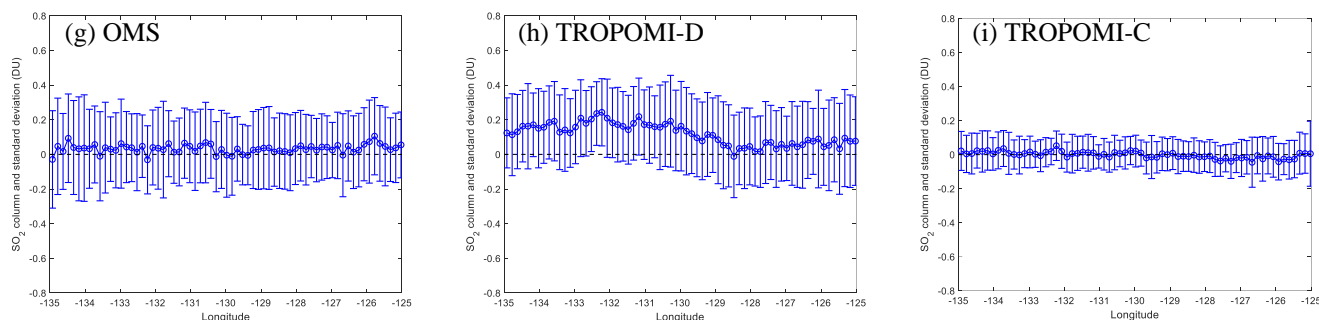


**Figure 9:** As Fig. 8 but for November 15, 2024. The missing pixels in the Figures b and c are caused by the gap between the two orbits and the Nan values in TROPOMI COBRA data.

350

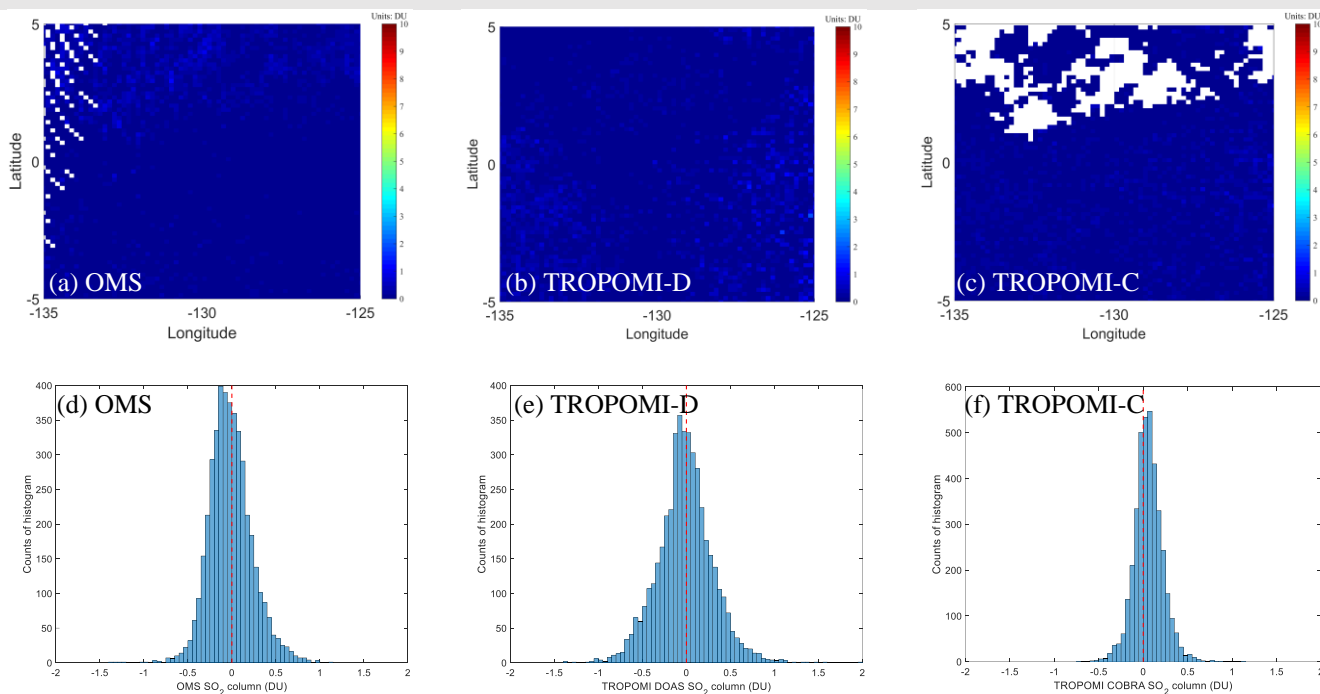
### Ocean-Area2, 20240823





**Figure 10:** As Fig. 8 but for region Ocean-Area 2 (latitude from 5°S to 5°N and longitude from 135°W to 125°W). The missing pixels in the Figure a are caused by low spatial resolution at the edges of the orbits, and the missing pixels in the Figure c are caused by the Nan values in TROPOMI COBRA data.

Ocean-Area2, 20241115



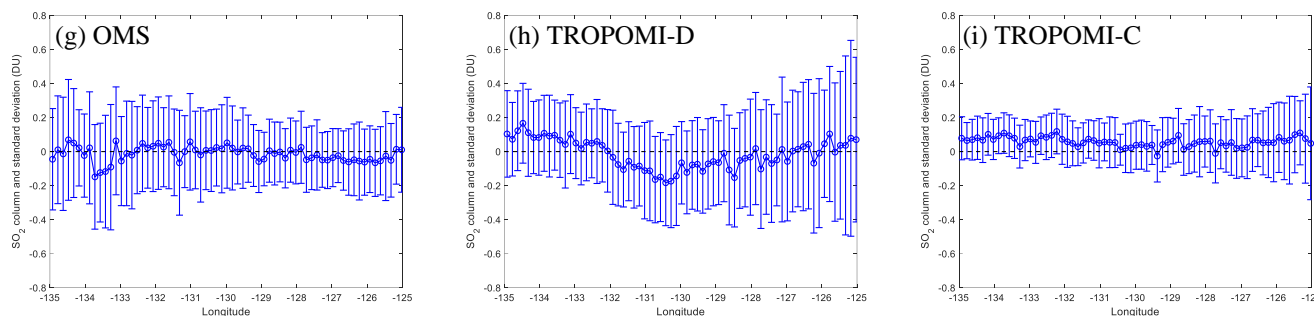


**Figure 11: As Fig. 10 but for November 15, 2024. The missing pixels in the Figure a are caused by low spatial resolution at the edges of the orbits, and the missing pixels in the Figure c are caused by the Nan values in TROPOMI COBRA data.**

## 4.2 Comparison over volcanic eruptions

355 The massive amounts of  $\text{SO}_2$  released over a short period during volcanic eruptions, as well as their long-distance transport and the subsequent formation of sulfate aerosols, not only influence the global radiative energy balance (McCormick et al., 1995) but also pose risks to aviation in the tropopause or stratosphere (Miller and Casadevall, 2000). Through the comparison in volcanic regions, the capability of OMS  $\text{SO}_2$  retrievals at large columns can be evaluated. In this section, we took the eruptions of Sundhnúkur volcano and Nyamuragira volcano as case studies for comparing FY3F/OMS  $\text{SO}_2$  with

360 TROPOMI DOAS and TROPOMI COBRA 7km  $\text{SO}_2$  results. To present the  $\text{SO}_2$  maps of OMS and TROPOMI DOAS more clearly, the resampling scheme in section 4.1 was not used in section 4.2. For TROPOMI DOAS, we used all pixels from the TROPOMI DOAS  $\text{SO}_2$  product instead of applying  $\text{QA} > 0.5$  to filter the high-quality pixels when comparing with the OMS  $\text{SO}_2$  results. The reason is that after applying the  $\text{QA} > 0.5$  filter, a lot of high  $\text{SO}_2$  pixels in TROPOMI DOAS over volcanic regions would be missing, making it difficult to compare with OMS  $\text{SO}_2$  results. In this section, TROPOMI COBRA L3 grid

365 7km  $\text{SO}_2$  products were used instead of COBRA PBL products.

The Sundhnúkur volcano is the first case study for comparing FY3F/OMS  $\text{SO}_2$  with TROPOMI DOAS and TROPOMI COBRA 7km  $\text{SO}_2$  results over a volcanic eruption. On August 22, 2024, Sundhnúkur volcano within the Reykjanes volcanic system began erupting and continued to emit  $\text{SO}_2$  for approximately 14 days (<https://volcano.si.edu/>). The eruption created a fissure approximately 3.9 km long, with lava and smoke reaching a height of about 1 km. The region of latitude from 55 °N to 65 °N and longitude from 30 °W to 5 °W was selected as the study area for the Sundhnúkur volcano. There are two OMS orbits (20240823\_1036 and 20240823\_1217) (Format: YYYYMMDD\_HHMM, UTC time of the first scan line) overpassing the Sundhnúkur volcano region on August 23, 2024. For the OMS orbit 20240823\_1217, most of the pixels covering the volcanic region are near the edge of the orbit where the measurement noise tends to be higher. For TROPOMI DOAS, although two orbits (20240823T125304 and 20240823T111134) (Format: YYYYMMDDTHHMMSS, observation start

375 UTC time) passed over the Sundhnúkur volcano area, only orbit 20240823T125304 is presented because most of its pixels over the Sundhnúkur volcano region were near the nadir of the orbit where the data quality is higher. As shown in Fig. 12,



both OMS and TROPOMI successfully captured the high SO<sub>2</sub> distribution around the Sundhnúkur volcano on August 23, 2024. The spatial distributions of OMS, TROPOMI DOAS and TROPOMI COBRA SO<sub>2</sub> over Sundhnúkur volcano are similar, but differ at the edge of the SO<sub>2</sub> plume. Compared with OMS orbit 20240823\_1036, orbit 20240823\_1217 has a local overpass time closer to that of TROPOMI orbit 20240823T125304 in the volcanic region, making the SO<sub>2</sub> results of OMS orbit 20240823\_1217 more consistent with those of TROPOMI orbit 20240823T125304. The correlation between OMS and TROPOMI DOAS reaches ~0.87 over the Sundhnúkur volcano on August 23, 2024, while the correlation between OMS and TROPOMI COBRA reaches ~0.76.

However, when SO<sub>2</sub> values exceed 50 DU, OMS SO<sub>2</sub> retrievals are significantly lower than those of TROPOMI DOAS over the Sundhnúkur volcano region on August 23, 2024. Moreover, the relative biases between OMS and TROPOMI DOAS increase with increasing SO<sub>2</sub> columns. This may be attributed to the reason that the OMS SO<sub>2</sub> retrieval uses the 312–326 nm fitting window, where SO<sub>2</sub> has strong absorption and is prone to saturation in the case of high SO<sub>2</sub> concentrations, leading to an underestimation of SO<sub>2</sub> columns. In order to mitigate the risk of saturation, TROPOMI DOAS uses two additional fitting windows (325–335 nm and 360–390 nm) (S5P-BIRA-L2-ATBD-400E) for volcanic eruption cases. In addition, the different overpass time of OMS and TROPOMI, along with varying volcanic eruption strength and meteorological conditions, may also be major contributors to the differences in SO<sub>2</sub> columns of OMS and TROPOMI DOAS. The TROPOMI COBRA SO<sub>2</sub> results retrieved from the 310.5–326 nm window are also lower than those from TROPOMI DOAS, but are more consistent with those from OMS.

The Nyamuragira volcano is the second case study for comparing FY3F/OMS SO<sub>2</sub> with TROPOMI DOAS and TROPOMI COBRA 7km SO<sub>2</sub> results over a volcanic eruption. Nyamuragira is Africa's most active volcano and a high-potassium basaltic shield volcano located in the eastern part of the Democratic Republic of the Congo, approximately 25 km north of Lake Kivu and 13 km north-northwest of the Nyiragongo volcano (<https://volcano.si.edu/>). Based on the Volcanic Explosivity Index (VEI) classification (Newhall and Self, 1982) and eruptive history reports of Nyamuragira from the Global Volcanism Program (GVP), the magnitude of Nyamuragira's eruptions can generally be classified as small to moderate. According to the GVP weekly reports, Nyamuragira had continuing eruptive activities in November 2024. In this section, the region of latitude from 10°S to 10°N and longitude from 15°E to 35°E was selected as the study area for the Nyamuragira volcano. The spatial distribution maps (Fig. 13) show that OMS, TROPOMI DOAS, and TROPOMI COBRA results clearly detected the high-concentration SO<sub>2</sub> plume from the Nyamuragira eruption, although the shape of the SO<sub>2</sub> plume differs due to differences in overpass time and observation angles. However, as shown in Fig. 14, most of OMS SO<sub>2</sub> retrievals over the Nyamuragira region are higher than the TROPOMI DOAS and TROPOMI COBRA results, which differs from the results for the Sundhnúkur volcano mentioned above. The reason may be attributed to factors such as the different retrieval fitting window and AMF strategies used by OMS SO<sub>2</sub>, TROPOMI DOAS and TROPOMI COBRA 7km SO<sub>2</sub>. It is worth noting that in Fig. 14, SO<sub>2</sub> column results from OMS and TROPOMI DOAS and TROPOMI COBRA were resampled to 0.15°×0.15° equal latitude-longitude grid, and only SO<sub>2</sub> retrievals greater than 1 DU within the Nyamuragira volcano region were selected and summed. For the case of the Nyamuragira volcano, which is located near the equator (unlike the high-latitude



Sundhnúkur volcano), it is difficult to find OMS and TROPOMI orbits with close overpass times. As a result of the overpass time differences between OMS and TROPOMI, the plume positions changed between the two measurements making direct comparison difficult.

From the above comparisons between FY3F/OMS SO<sub>2</sub> and TROPOMI DOAS and TROPOMI COBRA 7km SO<sub>2</sub> results, we can see that FY3F/OMS has the capability to monitor volcanic activities, and with high spatial resolution of 7 km × 7 km and a local overpass time different from TROPOMI, FY3F/OMS can contribute to a more effective satellite SO<sub>2</sub> product for the continuous monitoring of global volcanic activity.

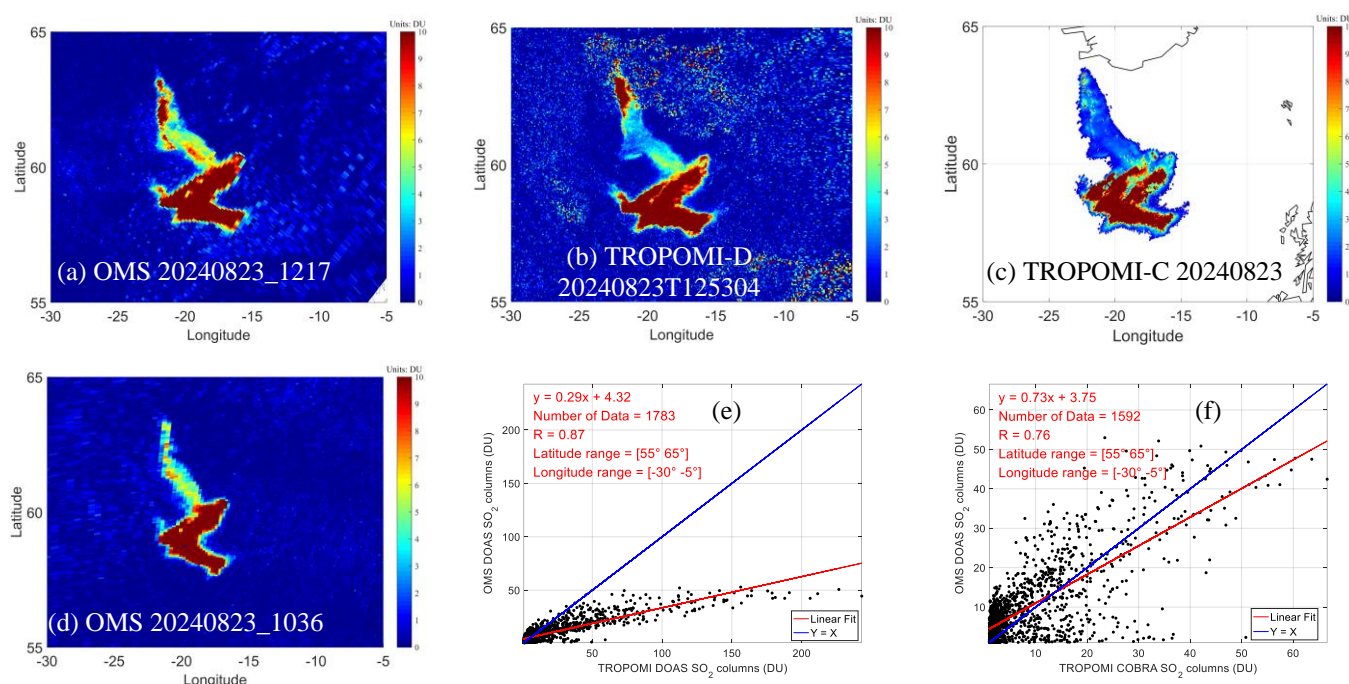


**Figure 12: SO<sub>2</sub> retrievals over Sundhnúkur volcano on August 23, 2024. (a, b, c, d) Spatial distribution of FY3F/OMS, TROPOMI DOAS and TROPOMI COBRA 7km SO<sub>2</sub> columns over Sundhnúkur volcano; (e, f) Scatter plots of OMS 20240823\_1217 and TROPOMI over Sundhnúkur volcano on August 23, 2024, where pixels with SO<sub>2</sub> columns greater than 1 DU were selected and TROPOMI is resampled to the latitude-longitude grid of OMS. The missing pixels in Figure a are the gap between the two OMS orbits, and the missing pixels in Figure c are the Nan values in TROPOMI COBRA data.**



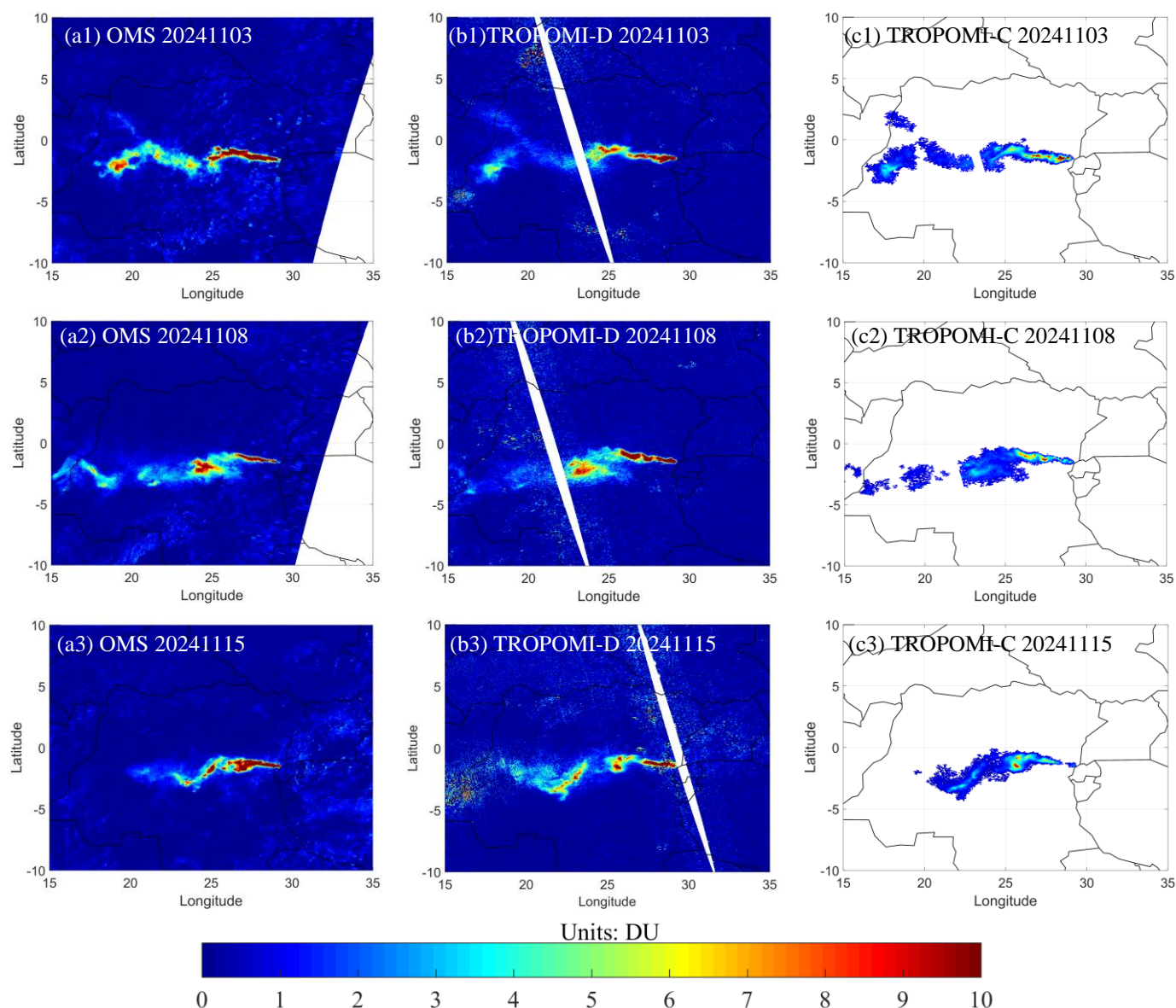


**Figure 13: SO<sub>2</sub> retrievals of OMS and TROPOMI over the Nyamuragira volcano on November 3, 8, and 15, 2024. The missing pixels are the gap between the two orbits, or the Nan values in TROPOMI COBRA data. (a1) OMS SO<sub>2</sub> columns, orbit 20241103\_0739; (b1) TROPOMI DOAS SO<sub>2</sub> columns, orbits 20241103T101246 (east) and 20241103T115416 (west); (c1) TROPOMI COBRA 7km L3 SO<sub>2</sub> columns, 20241103; (a2) OMS SO<sub>2</sub> columns, orbit 20241108\_0743; (b2) TROPOMI DOAS SO<sub>2</sub> columns, orbits 20241108T101829 (east) and 20241108T115958 (west); (c2) TROPOMI COBRA 7km L3 SO<sub>2</sub> columns, 20241108; (a3) OMS SO<sub>2</sub> columns, orbit 20241115\_0709; (b3) TROPOMI DOAS SO<sub>2</sub> columns, orbits 20241115T094602 (east) and 20241115T112732 (west); (c3) TROPOMI COBRA 7km L3 SO<sub>2</sub> columns, 20241115.**



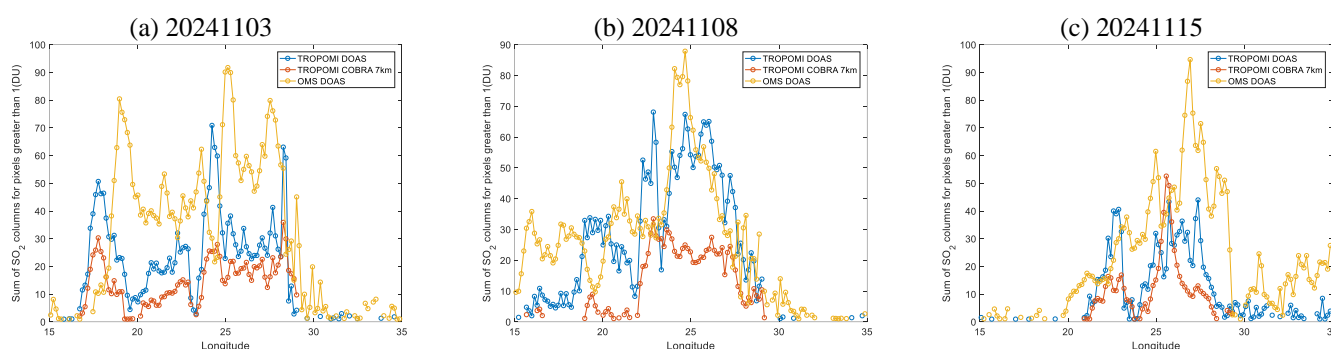


**Figure 14: Latitude-summed (latitude from 10°S to 10°N) SO<sub>2</sub> columns of OMS, TROPOMI DOAS and TROPOMI COBRA over Niyamuragira volcano on November 3, 8, and 15, 2024. Only pixels with SO<sub>2</sub> columns greater than 1 DU were selected.**

### 4.3 Comparison for anthropogenic emissions

Compared to the monitoring of high SO<sub>2</sub> emissions from natural sources such as volcanoes, the monitoring of anthropogenic SO<sub>2</sub> emissions from satellite observations is more challenging. Firstly, the atmospheric SO<sub>2</sub> from anthropogenic emissions is generally much lower compared to that of volcanic eruptions. Secondly, SO<sub>2</sub> from anthropogenic emission is primarily concentrated near the surface. However, the sensitivity of satellite measurements in the UV band near the surface is relatively low because solar UV radiation is partially absorbed and scattered by atmospheric components such as air, aerosols, and clouds during its transmission. As a result, the weakened UV radiation reaching the boundary layer reduces the sensitivity of satellite instruments to PBL SO<sub>2</sub> and makes it harder to distinguish SO<sub>2</sub> signals from background noise, especially at large solar zenith and satellite viewing angles.

Based on the SO<sub>2</sub> emission sources observed by TROPOMI in 2018 (Fioletov et al., 2020), we selected three representative regions – the Persian Gulf (oil and gas exploration), Norilsk (smelters), and Eastern India (power plants) – to compare three SO<sub>2</sub> column products: OMS SO<sub>2</sub>, TROPOMI DOAS SO<sub>2</sub>, and TROPOMI COBRA PBL SO<sub>2</sub>. These comparisons aim at evaluating the capability of OMS in monitoring SO<sub>2</sub> emissions from anthropogenic sources. Similar to the cases of volcanic eruptions, we used all pixels from the TROPOMI DOAS SO<sub>2</sub> product instead of applying QA > 0.5 to filter the high-quality pixels because the QA > 0.5 filter would remove many high SO<sub>2</sub> pixels over anthropogenic emission regions. In the case of anthropogenic emissions, TROPOMI COBRA L3 grid PBL SO<sub>2</sub> products were used for comparison instead of the COBRA 7km SO<sub>2</sub> products.

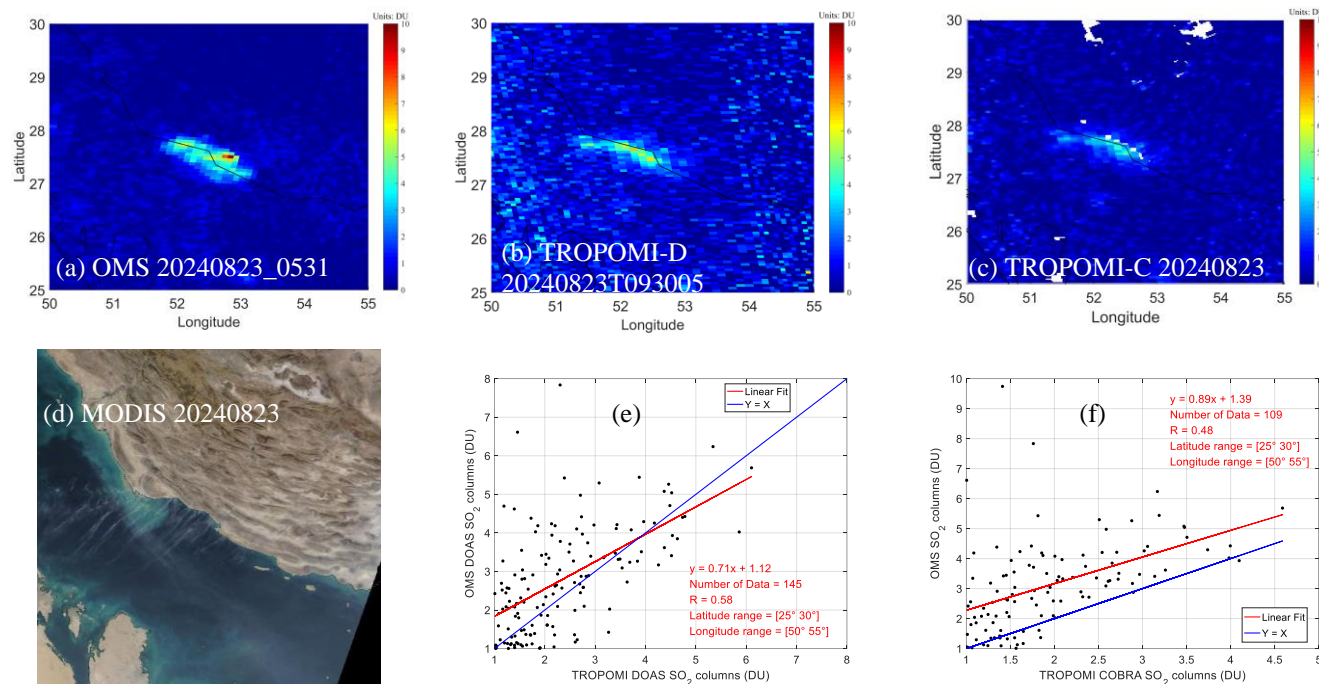
The Persian Gulf was selected due to its high anthropogenic emissions, including SO<sub>2</sub> and NO<sub>2</sub>, primarily from oil and gas extraction and refining industries (Mardani et al., 2025; Krotkov et al., 2016). This region has a higher probability of clear-sky days and is located in the low-latitude zone, which means relatively high SNR for satellite observations. As shown in Figs. 15 and 16, OMS effectively detects high SO<sub>2</sub> values over the Persian Gulf while maintaining a lower background noise.



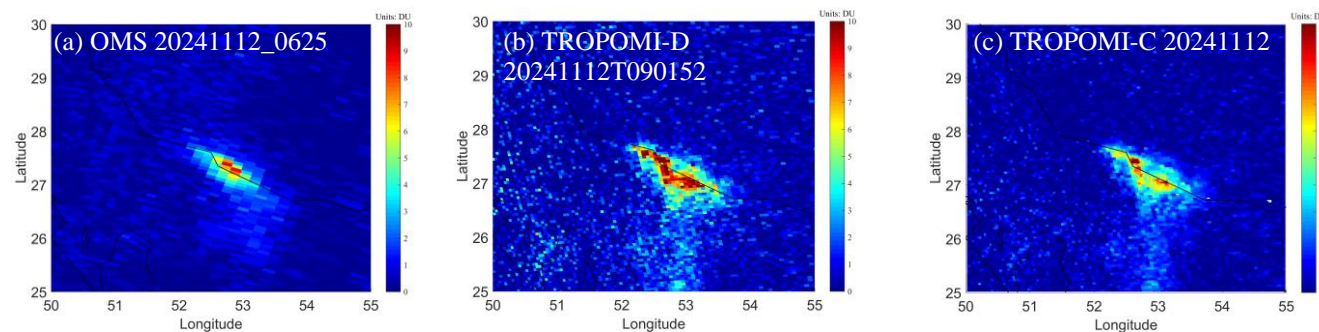
440 Scatter plots from different dates (August 23, 2024, and November 12, 2024) show that (1) The correlation coefficients between OMS and TROPOMI DOAS and TROPOMI COBRA SO<sub>2</sub> remain around 0.5–0.6; (2) TROPOMI COBRA SO<sub>2</sub> retrievals are lower than DOAS results over the Persian Gulf; (3) Additionally, the differences among the three datasets (OMS SO<sub>2</sub>, TROPOMI DOAS SO<sub>2</sub>, and TROPOMI COBRA PBL SO<sub>2</sub>) vary over time: on August 23, 2024, OMS SO<sub>2</sub> retrievals were higher than those from both TROPOMI DOAS and TROPOMI COBRA, whereas on November 12, 2024,  
445 OMS SO<sub>2</sub> retrievals were lower than those of TROPOMI DOAS and TROPOMI COBRA. This may be attributed to the factors such as viewing angle, overpass time, local emission variations, and AMF values.

Norilsk in northern Russia within the Arctic Circle is one of the world's biggest sources of anthropogenic SO<sub>2</sub> emissions due to its massive nickel and metal smelting industry (Bauduin et al., 2014). With winter lasting 6 to 9 months and snow covering the ground for most of the year, the region's low temperatures and atmospheric stability hinder pollutant dispersion,  
450 leading to persistently high SO<sub>2</sub> concentrations over Norilsk. Large SO<sub>2</sub> emissions cause severe air pollution and acid rain, which make Norilsk one of the most polluted cities in the world. On May 16, 2024, the orbits of OMS and TROPOMI with close local overpass times over Norilsk were selected to reduce the impact of emission and meteorological differences on the comparisons of SO<sub>2</sub> columns. As shown in Fig. 17, both OMS and TROPOMI were able to detect the SO<sub>2</sub> plumes over the Norilsk region. Note that for the OMS SO<sub>2</sub> retrievals over Norilsk on May 16, 2024, the constant AMF=2 was used for the  
455 conversion from SCD to VCD. The SO<sub>2</sub> columns from OMS and TROPOMI DOAS have a good correlation of 0.91–0.93 over the Norilsk region. In the case of Norilsk, OMS SO<sub>2</sub> retrievals are slightly lower than those from TROPOMI DOAS, with the average relative biases ( $|OMS - TROPOMI| / TROPOMI$ ) of the data from the Norilsk region in OMS orbit 20240516\_0334 being approximately 22% (excluding outliers with relative biases greater than 200% and SO<sub>2</sub> columns smaller than 1 DU), and for OMS orbit 20240516\_0516 being approximately 18% (applying the same filtering criteria). The  
460 TROPOMI COBRA PBL L3 products which have mostly Nan values over the Norilsk region are not presented in this section.

India's SO<sub>2</sub> emissions are mainly from coal fired power plants, transportation, and agricultural activities, which are growing rapidly, increasing by more than 100% from 2005 to 2015 (Krotkov et al., 2016; Kuttippurath et al., 2022). As shown in Fig. 18, OMS also successfully captured the high SO<sub>2</sub> plumes in Eastern India, but most of OMS SO<sub>2</sub> retrievals are lower than  
465 those from TROPOMI DOAS. This is mainly attributed to the simplified strategy of OMS using a constant AMF=1 for the Indian region. Future work will consider using Indian local SO<sub>2</sub> profiles to calculate specific AMFs over India in order to improve the accuracy of OMS SO<sub>2</sub> retrievals over this area. It is worth noting that the ranges of the color bars in Figs. 18a1–a3 are different from others to more clearly present the OMS SO<sub>2</sub> retrievals over Eastern India. Figure 18 also shows that due to different local overpass times, when the SO<sub>2</sub> pollution area in India is located at the edge of the TROPOMI orbit where  
470 large retrieval errors often occur, OMS can provide effective data support to fill the monitoring gaps caused by TROPOMI's edge-related pixels. These comparisons demonstrate that OMS can distinguish the effective daily SO<sub>2</sub> information from background noises.



**Figure 15: SO<sub>2</sub> retrievals over the Persian Gulf on August 23, 2024. (a, b, c) Spatial distribution of FY3F/OMS, TROPOMI DOAS and TROPOMI COBRA PBL SO<sub>2</sub> columns over Persian Gulf; (d) True Color Image of the Persian Gulf from Terra/MODIS (Source: <https://worldview.earthdata.nasa.gov/>); (e, f) Scatter plots of FY3F/OMS, TROPOMI DOAS and TROPOMI COBRA PBL SO<sub>2</sub> over the Persian Gulf on August 23, 2024, where pixels with SO<sub>2</sub> columns greater than 1 DU were selected and TROPOMI is resampled to the latitude-longitude grid of OMS. Note that the missing pixels in Figure c are the Nan values in TROPOMI COBRA data.**



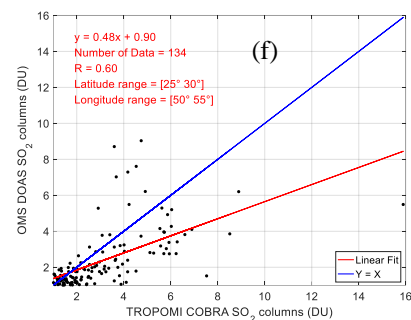
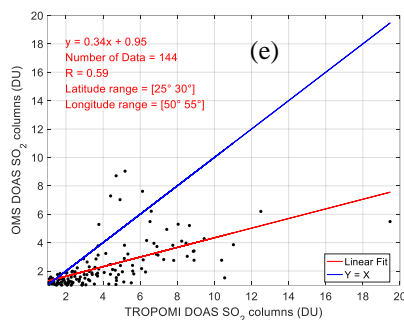
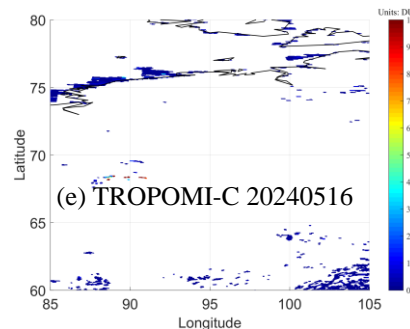
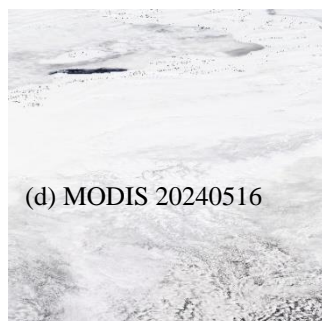
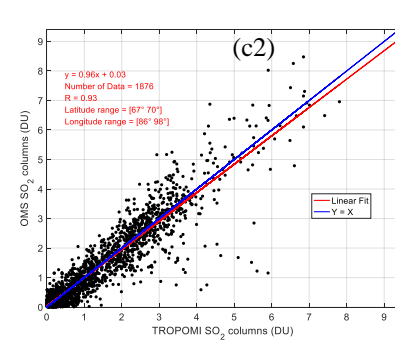
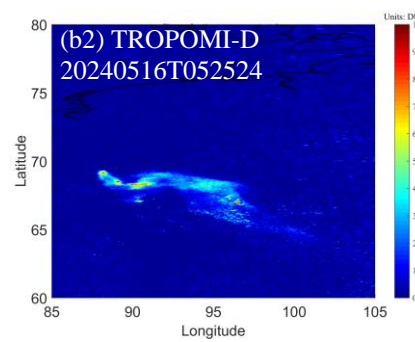
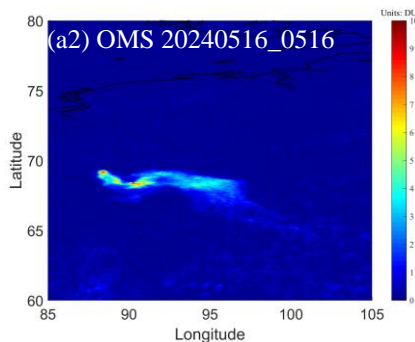
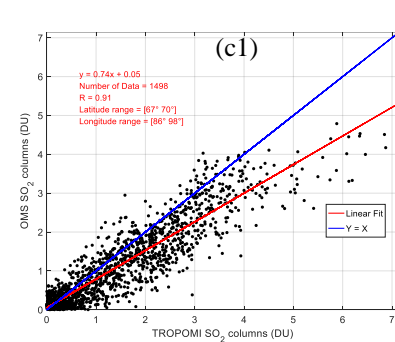
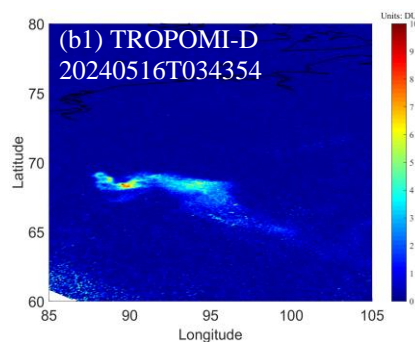
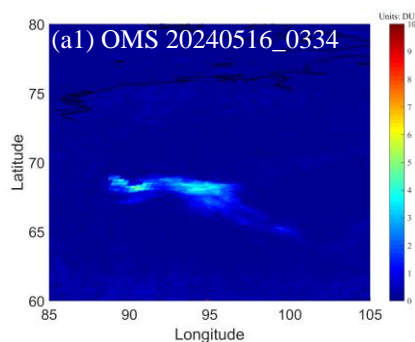


Figure 16: As Fig. 15 but for November 12, 2024.

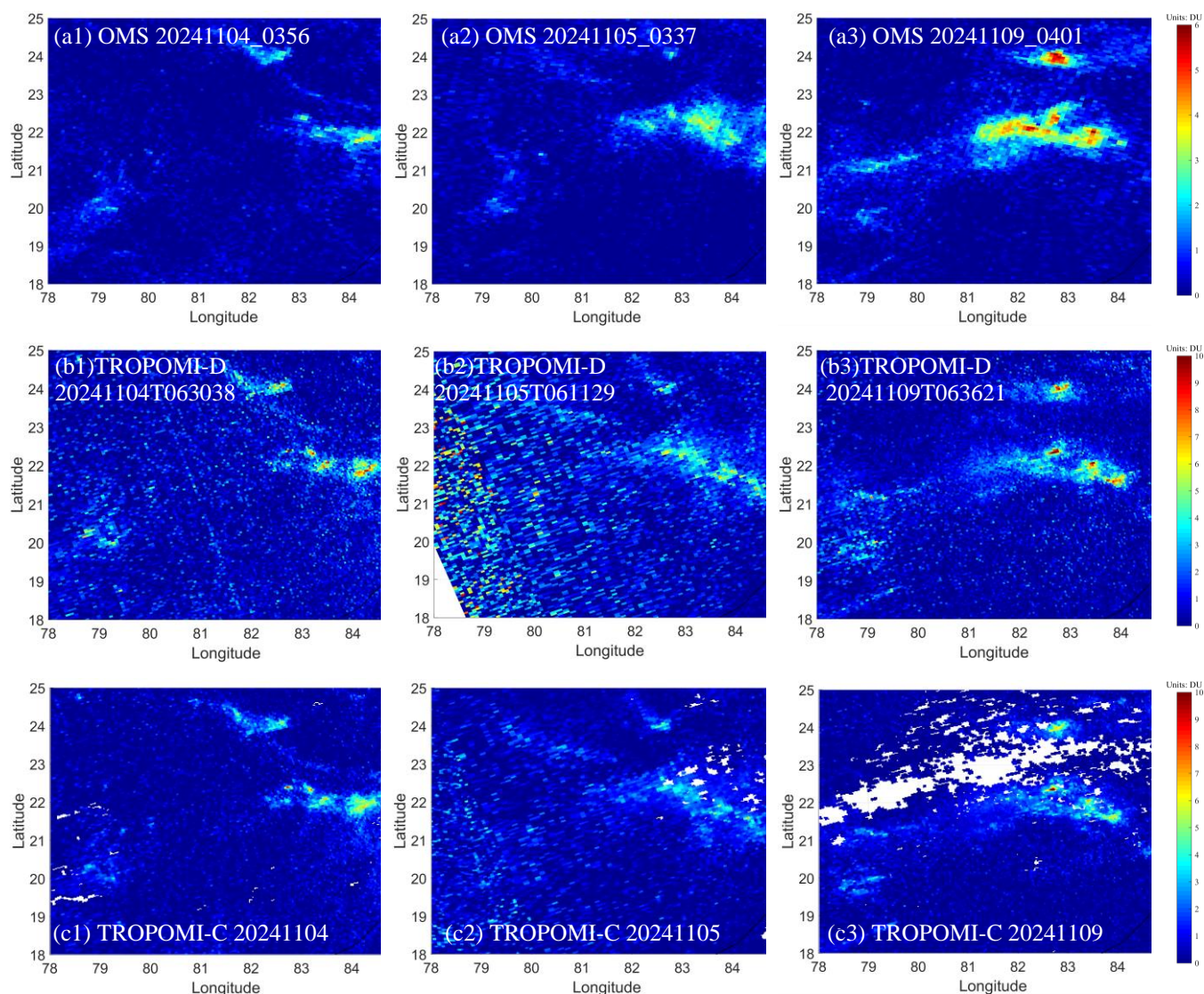
475







**Figure 17: SO<sub>2</sub> retrievals over Norilsk on May 16, 2024. (a1-2, b1-2) Spatial distribution of FY3F/OMS and TROPOMI DOAS SO<sub>2</sub> columns over Norilsk; (c1-2) Scatter plots of OMS and TROPOMI DOAS SO<sub>2</sub> columns over Norilsk on May 16, 2024, where pixels with SO<sub>2</sub> columns greater than 1 DU were selected and TROPOMI is resampled to the latitude-longitude grid of OMS; (d) True Color Image of Norilsk from Terra/MODIS on May 16, 2024; (e) SO<sub>2</sub> columns from TROPOMI COBRA PBL over Norilsk on May 16, 2024. Note that the missing pixels in Figure e are Nan values in TROPOMI COBRA data.**



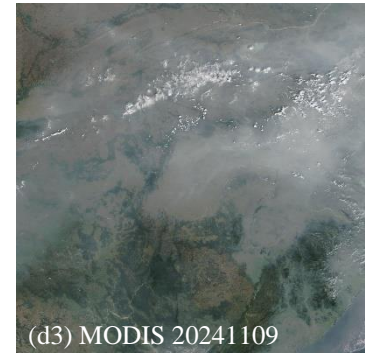
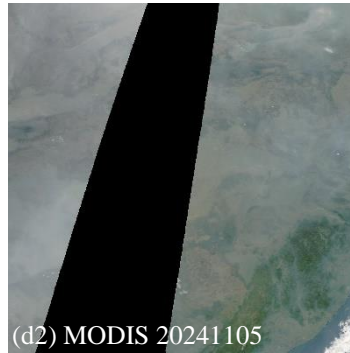


**Figure 18: SO<sub>2</sub> retrievals over Eastern India on November 4, 5, and 9, 2024. (a1-3, b1-3, c1-3) Spatial distribution of FY3F/OMS, TROPOMI DOAS and TROPOMI COBRA PBL SO<sub>2</sub> columns over Eastern India; (d1-d3) True Color Image of Eastern India from Terra/MODIS on November 4, 5, and 9, 2024. The missing pixels in the Figures c1-c3 are caused by Nan values in TROPOMI COBRA data.**

## 5 Error analysis

The main error sources in the OMS DOAS SO<sub>2</sub> retrieval include instrument-related errors, DOAS SCD spectral fitting errors, AMF uncertainties, and the residual error after background offset correction. Instrument-related errors include spectral and radiometric calibration errors, degradation of the instrument, stray light contamination and non-uniformity of the diffuser plate, which introduce systematic biases in both radiance and irradiance measurements. DOAS SCD spectral fitting errors include uncertainties in the absorption cross-sections of SO<sub>2</sub> and O<sub>3</sub>, interference from strong O<sub>3</sub> absorption, the Ring effect caused by inelastic scattering, and the selection of the polynomial order in spectral fitting which may introduce biases if not appropriately chosen. The AMF, which is crucial for the accuracy of SO<sub>2</sub> retrieval, is affected by the uncertainties in SO<sub>2</sub> vertical profile, surface reflectance, clouds and aerosols, and surface height. Moreover, the background offset correction may introduce additional uncertainties, especially in high SO<sub>2</sub> areas.

Considering these error sources and assuming that they are independent of each other, the total uncertainty in the retrieved SO<sub>2</sub> column can be approximated as:

$$\sigma_{SO_2} = \sqrt{\left(\frac{\sigma_{SCD}}{AMF}\right)^2 + \left(\frac{\sigma_{SCD}^{back}}{AMF}\right)^2 + \left(\frac{(SCD - SCD^{back}) \cdot \sigma_{AMF}}{AMF^2}\right)^2} \quad (\text{Eq. 2})$$

where  $\sigma_{SCD}$  is the random error from DOAS SO<sub>2</sub> SCD spectral fitting including instrument-related noise,  $\sigma_{SCD}^{back}$  is the residual systematic error after background offset correction, and  $\sigma_{AMF}$  is the AMF uncertainty which includes two components: one is related to the atmospheric scattering weight and the other one is associated with the SO<sub>2</sub> profile shape.

### 5.1 Errors in SCD retrieval

The errors in OMS irradiance and radiance measurements are one of the main error sources of SO<sub>2</sub> SCD retrievals. These errors significantly affect the accuracy of OMS SO<sub>2</sub> retrievals, and are the main causes of the systematic overestimation or





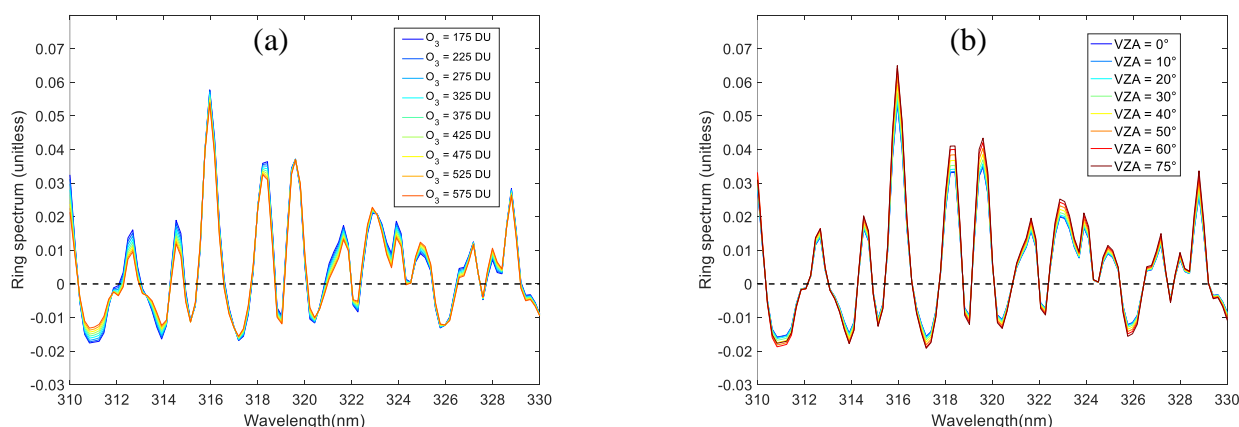
underestimation of SO<sub>2</sub> retrievals, such as along-track stripes at specific viewing angles and cross-track asymmetry in SO<sub>2</sub> SCD retrievals (Boersma et al., 2004). The OMS irradiance and radiance uncertainties mainly depend on viewing angle, wavelength, and optical degradation. The viewing angle dependence, caused by calibration inaccuracies, results in unequal responses for all viewing angles (one viewing angle corresponds to one cross-track position). With increasing optical degradation and inaccurate spectral calibration, more errors can be introduced into the irradiance and radiance spectra. This degradation is difficult to be monitored and calibrated, because no accurate standards over the full OMS wavelength range are readily available. Meanwhile, these errors in solar irradiance and earth radiance are not constant and can change with time and location, making it difficult to correct their impact on SO<sub>2</sub> retrievals. After one year in orbit, the intensity of OMS irradiance at the shorter wavelength of 317 nm has decreased by about 8.83%, while at the longer wavelength of 331 nm, it has decreased by about 6.07%. Using the TSIS HSRS hybrid solar reference spectrum instead of the OMS irradiance measurements can mitigate the impact of viewing angle dependence and degradation on OMS SO<sub>2</sub> retrieval. However, since the solar reference spectrum does not contain the instrument characteristics, it may introduce systematic overestimation or underestimation in SO<sub>2</sub> column retrievals. These systematic biases caused by the TSIS HSRS can be partially reduced through background offset correction but cannot be fully eliminated.

The temperature dependence and uncertainties of absorption cross-section spectra can affect the accuracy of DOAS SCD spectral fitting. The OMS SO<sub>2</sub> SCD retrieval utilizes the Bogumil SO<sub>2</sub> and O<sub>3</sub> absorption cross-section spectra at 273 K and 223 K for DOAS SCD fitting (Bogumil et al., 2003). However, the SO<sub>2</sub> and O<sub>3</sub> absorption cross-sections exhibit strong temperature dependence, which affects the accuracy of retrieved SO<sub>2</sub> SCDs when using the constant 273 K SO<sub>2</sub> and 223 K O<sub>3</sub> absorption cross-sections. The SO<sub>2</sub> SCD retrievals increase accordingly as higher-temperature absorption cross-sections are used (Yan et al., 2014). The differences in SCD retrievals caused by temperature-dependent absorption cross-sections increase with increasing SO<sub>2</sub> columns. For example, compared to SCD retrievals using the 203K absorption cross-sections, the differences in SO<sub>2</sub> SCDs can reach a maximum of ~25 DU (with SCDs around 60 DU) (Yan et al., 2014). In addition to the temperature dependence, the uncertainty of the SO<sub>2</sub> and O<sub>3</sub> absorption cross-sections is also one of the error sources in the SO<sub>2</sub> SCD retrievals. Systematic errors in slant columns due to SO<sub>2</sub> cross-section uncertainties are estimated to be around 6% in the 312–326 nm fitting window (Vandaele et al., 2009). The uncertainty of the SO<sub>2</sub> absorption cross-sections from Bogumil et al. (2003) varies with temperature, being 2.8% at 293 K and 3.0% at lower temperatures. The uncertainty of O<sub>3</sub> absorption cross-sections from Bogumil et al. (2003) is approximately 3.1% or less. Therefore, to improve the accuracy of OMS SO<sub>2</sub> retrievals, it is essential to account for the variations in the SO<sub>2</sub> absorption cross-section with temperature and altitude, especially in cases of volcanic eruptions. Future work will incorporate accurate and real-time temperature and SO<sub>2</sub> profile data to account for temperature-dependent effects in OMS SO<sub>2</sub> retrievals.

In the UV wavelength band, the Ring effect is a non-negligible part of the DOAS SCD fitting process. In this study, one single Ring spectrum simulated with the SCIATRAN model was used to retrieve OMS SO<sub>2</sub> for all pixels. As shown in Fig. 19, the Ring spectrum convolved with the OMS ISRF varies with SZA, VZA, O<sub>3</sub> column and AS within the 310–330 nm wavelength range. The variation of the Ring spectrum with RAA is negligible and is not presented in this study. The mean



percentage change in the Ring spectrum is approximately 27.67% (absolute deviation: 0.0025) as the  $O_3$  column varies from 175 DU to 575 DU, 47.34% (absolute deviation: 0.0048) as the AS varies from 0 to 1, 24.18% (absolute deviation: 0.0021) as the VZA varies from  $0^\circ$  to  $75^\circ$ , and 45.29% (absolute deviation: 0.0047) as the SZA varies from  $0^\circ$  to  $80^\circ$ . Although the Ring spectrum varies significantly with SZA, VZA,  $O_3$  column, and AS within the 310–330 nm wavelength range, its impact on  $SO_2$  retrievals is relatively small for high  $SO_2$  concentrations due to the weak correlation between the Ring spectrum and the satellite TOA reflectance. However, for low  $SO_2$  concentrations, the influence is non-negligible. Additionally, the accuracy of DOAS SCD fitting is also influenced by the following factors: (1) Interference from strong  $O_3$  absorption in the retrieval fitting window. Due to the overlap of  $O_3$  and  $SO_2$  absorption in the UV wavelength and the fact that the atmospheric  $O_3$  absorption is often much higher than that of  $SO_2$ , the UV radiation reaching the near-surface (the primary altitude of anthropogenic  $SO_2$  emissions) is weakened, resulting in a lower SNR. When using the weakened radiance and DOAS fitting to simultaneously retrieve  $O_3$  and  $SO_2$ , the strong  $O_3$  absorption signal may overshadow the  $SO_2$  absorption information, leading to errors in the DOAS  $SO_2$  SCD retrievals. Sensitivity analysis shows that a 1% increase in  $O_3$  can lead to approximately a 5% decrease in DOAS  $SO_2$  retrievals (Yan et al., 2017). (2) Selection of retrieval fitting window. Different retrieval fitting windows have varying  $SO_2$  absorption features,  $O_3$  absorption interference, and SNR. The scheme using a single retrieval fitting window of 312–326 nm for OMS  $SO_2$  SCD retrieval may lead to the underestimation of  $SO_2$  columns in the cases of volcanic eruptions or high-reflectivity surfaces. However, employing multiple fitting windows may lead to inconsistencies among results from different retrieval fitting windows. (3) Low-order polynomial. In DOAS retrievals, low-order polynomials are used to remove slow-varying components, such as aerosol scattering and broad spectral features of absorption. If the polynomial order is too low, it may fail to effectively remove slow-varying components, while if it is too high, overfitting may occur, leading to partial removal of the true  $SO_2$  signal. These errors in SCD propagate into the final OMS  $SO_2$  VCD results, degrading the accuracy and applicability of the OMS  $SO_2$  product.



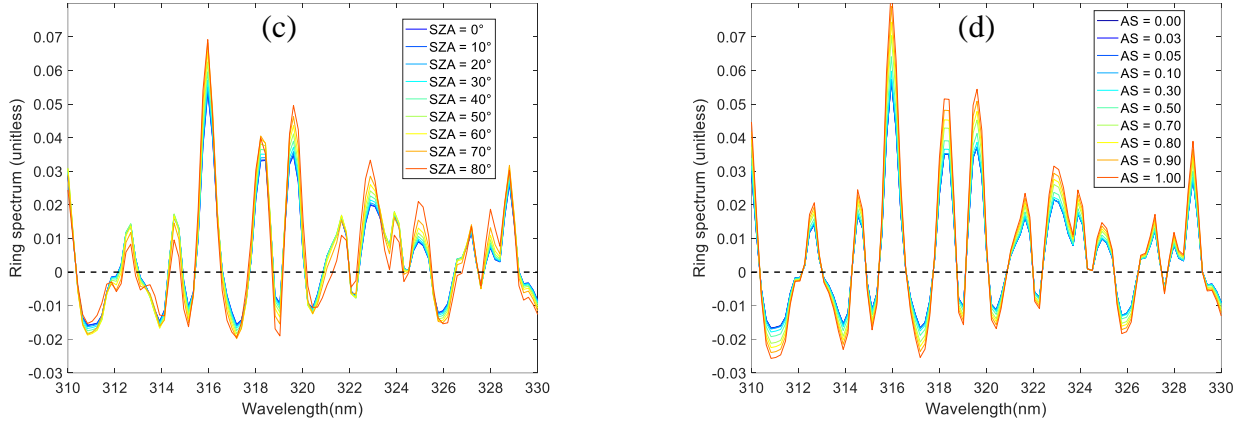


**Figure 19: Variation of Ring spectrum with O<sub>3</sub>, VZA, SZA and surface reflectivity (AS). Ring spectrum was calculated with the SCIATRAN model, convolved with the OMS ISRF. The default SCIATRAN settings for the Ring spectrum are as follows: wavelength step=0.2 nm, clear sky, HS=0 km, O<sub>3</sub>=275 DU, AS=0.05, SZA=30°, VZA=0°, RAA=0°.**

## 5.2 Errors from AMF

The AMF is also one of the primary error sources of OMS SO<sub>2</sub> VCD retrieval. It is typically computed as the weighted average of altitude-dependent Box-AMFs (equivalent to scattering weights) across all layers, with the weights determined by the SO<sub>2</sub> distribution in each layer (Eq. 3) (Chen et al., 2009; Wagner et al., 2007; Palmer et al., 2001; Boersma et al., 2004):

$$AMF = \sum_i \text{Box-AMF}_i \times \frac{c_i \Delta h_i}{\sum_j c_j \Delta h_j} \quad (\text{Eq. 3})$$

Where  $c_i$  represents the SO<sub>2</sub> number density in the  $i$ -th layer, and  $\Delta h_i$  denotes the thickness of that layer.

Box-AMFs quantify the contribution of each atmospheric layer to the total AMF and allows for flexible updates of AMF with new SO<sub>2</sub> profiles, eliminating the procedure of rebuilding the AMF lookup table. In this study, due to the difficulty in obtaining accurate and satellite-synchronized global SO<sub>2</sub> profiles, two AMF constants under typical conditions were used to convert the OMS SO<sub>2</sub> SCD to VCD (see section 3.5 for more information).

However, due to the heterogeneity of the global land cover and the variability of atmospheric conditions and SO<sub>2</sub> emission sources, the approximation using constant AMFs can introduce large uncertainties into the final SO<sub>2</sub> VCD retrieval. The AMF value is influenced by multiple factors including wavelength, SZA, VZA, RAA, AS, HS (also referred to as terrain height), O<sub>3</sub> column, SO<sub>2</sub> vertical profile shape, and cloud fraction and altitude (Lee et al., 2009). To analyze the impact of these factors on AMF calculation, we used the SCIATRAN as forward radiative transfer model (Rozanov et al., 2005) to compute Box-AMF under different forward model settings. Box-AMFs corresponding to each set of forward input settings are stored as a function of altitude, representing the atmospheric contribution from each layer.

Figure 20 illustrates the variation of SCIATRAN Box-AMF with SZA, VZA, RAA, AS, HS, wavelength, and O<sub>3</sub> column. The forward model settings remain consistent across all cases, except for the variable being analyzed: SZA = 32.9°, VZA = 0°, RAA = 0°, LER AS = 0.05, HS = 0 km, wavelength = 320 nm, O<sub>3</sub> column = 365 DU, clear sky, and with the assumption



of surface reflectance as LER. As shown in Figs. 20a-b, at lower altitudes, Box-AMF is relatively insensitive to changes in SZA and VZA within the range of 0–50°. However, at higher altitudes (e.g., above 5 km), the Box-AMF generally increases with increasing SZA and VZA due to the longer atmospheric path length at larger angles, which enhances the contribution of each atmospheric layer to the total AMF. Note that when SZA or VZA is greater than 73.5°, the Box-AMF has a significant decrease below altitude 10 km compared to the values at other angles. As shown in Fig. 20c, the variation of Box-AMF with RAA is negligible. Box-AMF increases as surface reflectance increases (Fig. 20d) due to higher reflectivity enhancing atmospheric multiple scattering, which increases the photon path length and thereby raises Box-AMF values. When LER surface reflectance changes from 0 to 1, the surface Box-AMF increases from 0.23 to 4.14, an increase of approximately 1700%. However, the increase of surface reflectance also changes the vertical shape of Box-AMF, shifting it from increasing with altitude to decreasing with altitude. Fig. 20e shows that the Box-AMF decreases with increasing terrain height, as higher surface elevation reduces the atmospheric column above the ground, leading to less scattering and decreased sensitivity. The variation of Box-AMF with wavelength ranging from 310 nm to 330 nm (Fig. 20f) shows that Box-AMF increases with increasing wavelength. The difference in Box-AMF at different wavelengths varies with altitude. For example, near the surface, when the wavelength increases from 310 nm to 330 nm, the surface Box-AMF increases from 0.28 to 0.48, a rise of 71.13%; At an altitude of 10 km, the Box-AMF increases from 1.69 to 2.36, a rise of 39.57%. Note that for most cases in this study, the wavelength 320 nm, which is approximately at the center of the SO<sub>2</sub> retrieval window (312–326 nm), was chosen to perform the SCIATRAN Box-AMF calculation. The variation of Box-AMF with the O<sub>3</sub> column from 125 DU to 575 DU (Fig. 20g) shows that, compared to other influencing factors, O<sub>3</sub> column has a relatively weak impact on Box-AMF, especially for altitudes below 5 km. The Box-AMF gradually decreases as the O<sub>3</sub> column increases. The differences in Box-AMF under different O<sub>3</sub> column conditions are more noticeable between altitudes of 5 km and 25 km. For example, at an altitude of 15 km, Box-AMF decreases from 2.41 to 2.07 as the O<sub>3</sub> column increases from 125 DU to 575 DU, a decrease of about 14%.

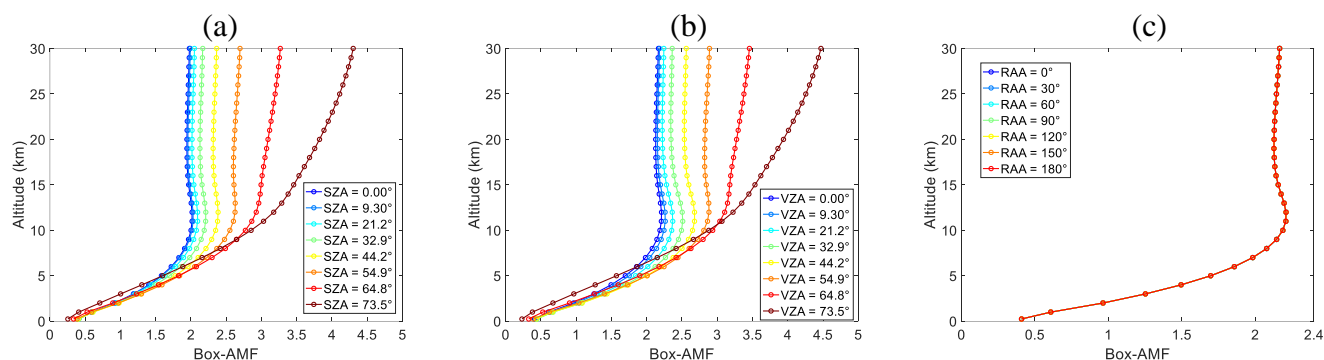
As seen from the above results, compared to other influencing factors, surface reflectance has a relatively strong impact on Box-AMF, thus affecting the accuracy of AMF calculations, especially in anthropogenic emission regions where SO<sub>2</sub> is concentrated near the surface. The errors of Box-AMF from surface reflectance primarily come from two aspects. One is the errors in the surface reflectance climatology. In many satellite products, for each pixel, a surface reflectance climatology (such as from OMI (Kleipool et al., 2008) or TROPOMI (Tilstra et al., 2024)) is interpolated to obtain the corresponding surface reflectance, which is then used as input to calculate the corresponding Box-AMF. The uncertainties in the surface reflectance climatology and interpolation errors due to the spatial resolution differences between the satellite observations and surface reflectance climatology can degrade the accuracy of the Box-AMF calculations. The sensitivity analysis of AS error on SCIATRAN Box-AMF (Fig. 21), which was conducted by introducing a 1% and 0.01 perturbation in AS values ranging from 0.01 to 0.90, shows that (1) The uncertainties in Box-AMF due to a 1% and 0.01 AS variation show a decreasing trend with increasing altitude, meaning that Box-AMF is more sensitive to AS at lower altitudes. (2) The uncertainties of Box-AMF due to a 1% AS variation increase as the AS increases, while those due to a 0.01 AS variation



decrease as the AS increases. When AS is small (e.g., AS = 0.01, 0.03, 0.05), a 1% variation in AS can lead to less than a 0.5% change in Box-AMF near the surface. However, when AS ranges from 0.8 to 0.9, the uncertainties of Box-AMF due to a 1% AS variation can reach up to 1.1%-1.2% near the surface. Another aspect affecting the accuracy of Box-AMF due to surface reflectance is the assumption of surface reflectance as LER during SCIATRAN Box-AMF calculation. Surface reflectivity, which depends on the surface properties and the geometry of incident and reflected light, is not uniformly distributed in all directions (i.e., anisotropy). This anisotropy is typically described by the bidirectional reflectance distribution function (BRDF). However, due to more scattering in the UV, this effect is more relevant at longer wavelengths. Therefore, accurate AS input is crucial for the accuracy of Box-AMF calculation, especially in regions with high surface reflectance.

As shown in Eq. 3, the shape of the SO<sub>2</sub> vertical profile is important for the calculation of AMF. Since the actual vertical distribution of atmospheric SO<sub>2</sub> is often difficult to get, a priori profiles from models are commonly used in AMF calculations. For regions with anthropogenic emissions, atmospheric chemistry models like GEOS-Chem and TM5 are often used to provide global SO<sub>2</sub> profiles for AMF calculation. The uncertainties in the SO<sub>2</sub> vertical profile can introduce errors into AMF calculations. In future work, we aim to incorporate high-resolution and satellite-synchronized SO<sub>2</sub> vertical profiles to improve the accuracy of AMF.

Additionally, for SO<sub>2</sub> retrievals from high spatial resolution satellite observations, it is often necessary to build a Box-AMF lookup table (LUT) by using radiative transfer model that considers variables such as SZA, VZA, RAA, AS, HS, wavelength, O<sub>3</sub> column, and cloud cover. The corresponding Box-AMF values for each satellite observation pixel are then obtained through interpolation within the LUT. This approach significantly improves the efficiency of retrieval, avoiding excessive computational time that would result from repeatedly running the radiative transfer model. However, the LUT approach may introduce new errors into the Box-AMF results. First, LUT are typically constructed based on specific atmospheric conditions and forward input parameters, which may not accurately represent real atmospheric conditions. Secondly, the interpolation process within the LUT introduces further uncertainties into the Box-AMF results.



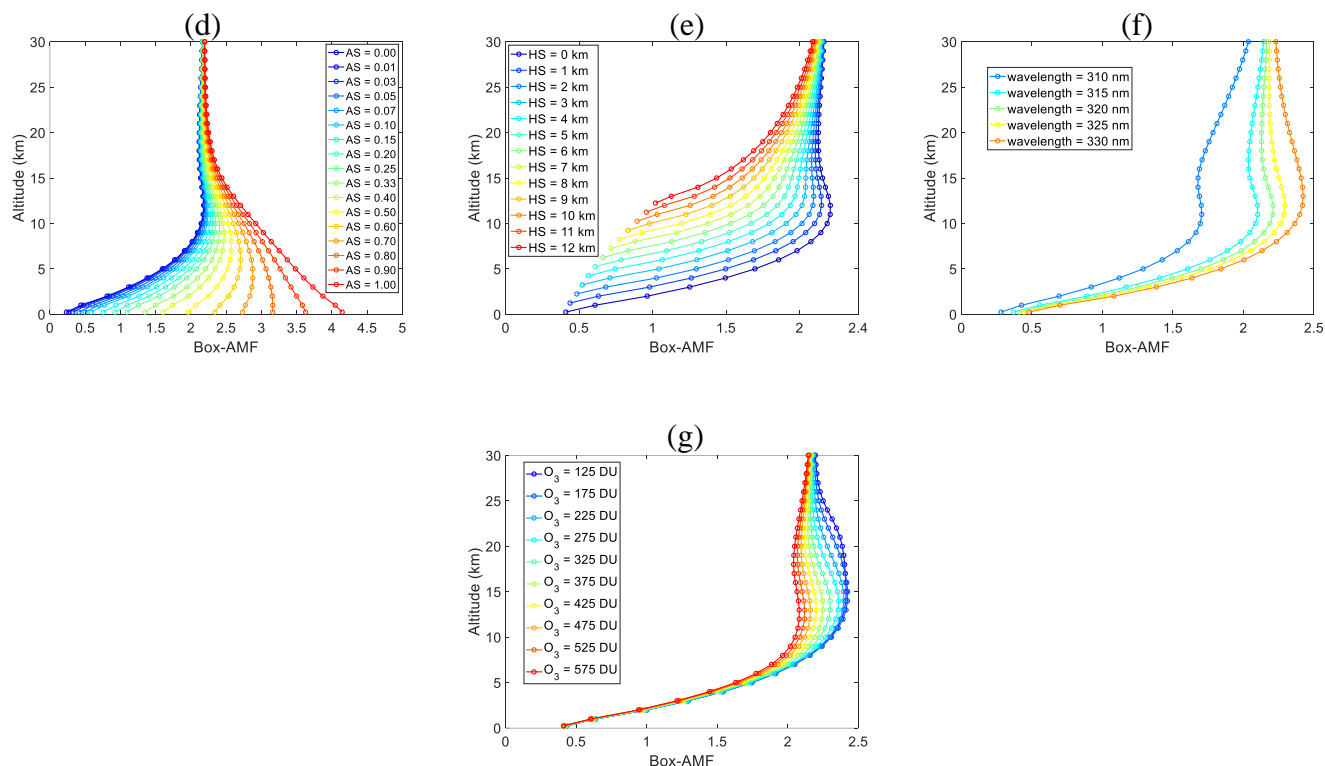


**Figure 20: Variation of Box-AMF with SZA, VZA, RAA, AS, HS, wavelength, and O<sub>3</sub> column. The default SCIATRAN settings for Box-AMF calculation are as follows: wavelength=320 nm, clear sky, HS=0 km, O<sub>3</sub>=275 DU, AS=0.05, SZA=32.9°, VZA=0°, RAA=0°.**

630

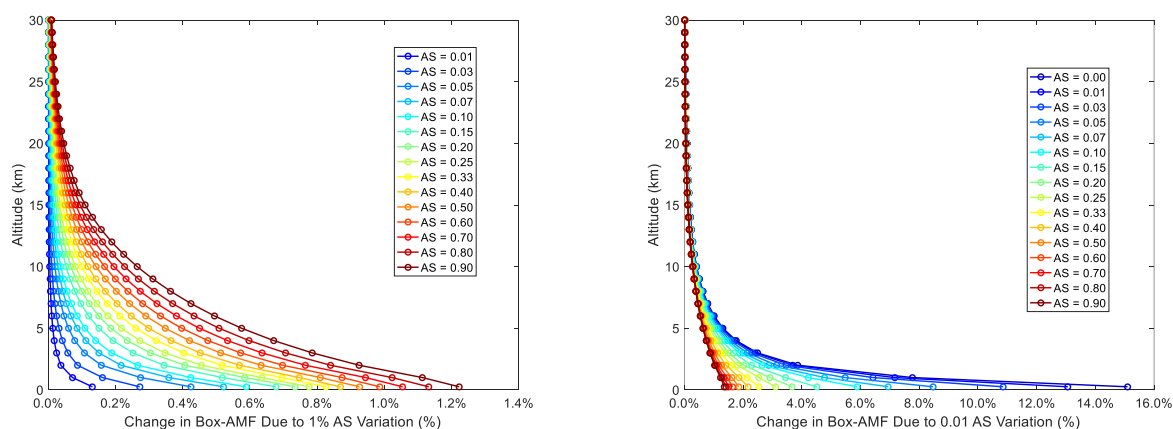


**Figure 21: Sensitivity analysis of AS error on SCIATRAN Box-AMF calculation. The other default SCIATRAN settings for Box-AMF calculation are as follows: wavelength=320 nm, clear sky, HS=0 km, O<sub>3</sub>=275 DU, SZA=32.9°, VZA=0°, RAA=0°.**





### 5.3 Errors from background offset correction

Background offset correction is essential for the initial SO<sub>2</sub> column retrievals from satellite observations which usually have systematic overestimation or underestimation problems. However, it is hard to get the accurate background offset for SO<sub>2</sub> retrieval of each pixel. In this study, an iterative sliding correction scheme for background offset correction was applied to initial OMS SO<sub>2</sub> retrievals, with the purpose of forcing SO<sub>2</sub> values over clean or low SO<sub>2</sub> emission regions to zero. This approach helps addressing problems such as along-track stripes and cross-track asymmetry. However, the sliding window strategy assumes that pixels with values smaller than the threshold (2 DU) within the sliding window represent zero SO<sub>2</sub> emissions, which may lead to a loss of SO<sub>2</sub> information contained in the low-emission regions. This not only could limit the applicability of the OMS SO<sub>2</sub> product for monitoring anthropogenic emission sources, but also may lead to many negative retrievals of SO<sub>2</sub> column in clean regions. Furthermore, SO<sub>2</sub> retrievals at certain cross-track positions (assumed to be clean near-zero) may exceed the 2 DU threshold, requiring the threshold to be adjusted upwards to achieve a better effect after background offset correction. Therefore, although the current sliding window strategy helps mitigate background errors, it may also affect the accuracy of OMS SO<sub>2</sub> column retrievals.

### 6 Conclusions and future work

This study utilized TOA reflected radiance data from the Chinese FY3F/OMS-N instrument, launched in August 2023 to retrieve global SO<sub>2</sub> columns with a DOAS approach. Based on the characteristics of the OMS instrument and the performance of its L1 data, specific schemes including solar spectrum selection, spectral soft calibration, and background offset correction were developed to effectively reduce along-track stripes and across-track asymmetry in the initial OMS SO<sub>2</sub> retrievals. The OMS SO<sub>2</sub> retrievals were compared with TROPOMI DOAS and TROPOMI COBRA SO<sub>2</sub> products in clean oceanic regions, under volcanic eruption conditions, and in anthropogenic emission regions. The comparison results indicate that OMS retrievals show good stability in clean oceanic regions and have the capability to monitor SO<sub>2</sub> emissions from volcanic eruptions and anthropogenic sources. In particular, for high-latitude regions with large observation angles (Norilsk region), FY3F/OMS can clearly capture the SO<sub>2</sub> plumes from anthropogenic emissions. Overall, with its high spectral and spatial resolution, morning overpass time, daily global coverage, and reliable SO<sub>2</sub> retrieval results, OMS will provide effective data support for monitoring the continuous SO<sub>2</sub> changes from global volcanic eruptions and anthropogenic activities, helping to fill the spatial and temporal gaps in the existing global satellite network.

The current OMS SO<sub>2</sub> retrievals still have several shortcomings that need to be addressed in the future. Due to the lack of a prior SO<sub>2</sub> and temperature profiles, a simplified approach that uses two constant AMF values for typical conditions was applied for the OMS SO<sub>2</sub> conversion from SCD to VCD in this study. More work will be needed to incorporate accurate and satellite-synchronized SO<sub>2</sub> vertical profiles to improve the accuracy of AMF. Another issue that needs to be addressed in the future is the simultaneous retrieval of volcanic eruption heights, which would help improve the accuracy of SO<sub>2</sub> retrievals in volcanic regions. Additionally, the 312–326 nm retrieval fitting window used in the OMS SO<sub>2</sub> product exhibits nonlinear



variation in the case of very large SO<sub>2</sub> concentrations, leading to an underestimation of SO<sub>2</sub> columns. In the future, SO<sub>2</sub> retrievals from longer UV wavelength fitting windows or nonlinear spectral fitting or correction factors varying with SO<sub>2</sub> columns will be incorporated into the operational OMS SO<sub>2</sub> products to mitigate the saturation issue in the case of large volcanic eruptions.

Furthermore, although in this study the comparison between OMS SO<sub>2</sub> retrievals and TROPOMI SO<sub>2</sub> products was conducted to demonstrate the capability of OMS SO<sub>2</sub> retrievals, synchronous and high-quality ground-based or airborne measurements remain crucial for validating the accuracy of OMS SO<sub>2</sub> retrievals. In the future, ground-based and airborne experiments need to be conducted to provide accurate ground-based or airborne data for the validation of OMS SO<sub>2</sub> retrievals.

### Data Availability

The SO<sub>2</sub> data produced in this study is available from the authors on request. FY3F/OMS-N L1 data can be downloaded from the website <http://data.nsmc.org.cn/DataPortal/en/home/index.html>. TROPOMI DOAS SO<sub>2</sub> data is available via the Copernicus Data Space Ecosystem (<https://browser.dataspace.copernicus.eu/>). TROPOMI COBRA SO<sub>2</sub> data is available via the PAL system (<https://data-portal.s5p-pal.com/products/so2cbr.html>).

### Acknowledgements

This study has been supported by the National Key Research and Development Program of China under Grant 2022YFB3904801. The authors wish to thank the many scientists and engineers from FY3F/OMS L1 team, TROPOMI team, and the Institute of Environmental Physics at the University of Bremen. The authors also acknowledge the use of ChatGPT for improving the English of the manuscript.

### References

- Bauduin, S., Clarisse, L., Clerbaux, C., Hurtmans, D., and Coheur, P. F.: IASI observations of sulfur dioxide (SO<sub>2</sub>) in the boundary layer of Norilsk, *J Geophys Res-Atmos*, 119, 4253-4263, 2014.
- Boersma, K., Eskes, H., and Brinksma, E.: Error analysis for tropospheric NO<sub>2</sub> retrieval from space, *J Geophys Res-Atmos*, 109, 2004.
- Bogumil, K., Orphal, J., Homann, T., Voigt, S., Spietz, P., Fleischmann, O. C., Vogel, A., Hartmann, M., Kromminga, H., Bovensmann, H., Frerick, J., and Burrows, J. P.: Measurements of molecular absorption spectra with the SCIAMACHY pre-flight model: instrument characterization and reference data for atmospheric remote-sensing in the 230–2380 nm region, *Journal of Photochemistry and Photobiology A: Chemistry*, 157, 167-184, 10.1016/s1010-6030(03)00062-5, 2003.



- Burrows, J. P., Weber, M., Buchwitz, M., Rozanov, V., Ladstätter-Weissenmayer, A., Richter, A., DeBeek, R., Hoogen, R., Bramstedt, K., Eichmann, K. U., and Eisinger, M.: The global ozone monitoring experiment (GOME): Mission concept and first scientific results, *J Atmos Sci*, 56, 151-175, Doi 10.1175/1520-0469(1999)056<0151:Tgomeg>2.0.Co;2, 1999.
- Carn, S. A., Krueger, A. J., Krotkov, N. A., Yang, K., and Evans, K.: Tracking volcanic sulfur dioxide clouds for aviation hazard mitigation, *Nat Hazards*, 51, 325-343, DOI 10.1007/s11069-008-9228-4, 2009.
- Carn, S. A., Krueger, A. J., Krotkov, N. A., Yang, K., and Levelt, P. F.: Sulfur dioxide emissions from Peruvian copper smelters detected by the Ozone Monitoring Instrument, *Geophys Res Lett*, 34, 1093-1101, 10.1029/2006gl029020, 2007.
- Carn, S. A., Strow, L. L., de Souza-Machado, S., Edmonds, Y., and Hannon, S.: Quantifying tropospheric volcanic emissions with AIRS: The 2002 eruption of Mt. Etna (Italy), *Geophys Res Lett*, 32, Artn L02301  
Doi 10.1029/2004gl021034, 2005.
- Chance, K. V. and Spurr, R. J.: Ring effect studies: Rayleigh scattering, including molecular parameters for rotational Raman scattering, and the Fraunhofer spectrum, *Appl Optics*, 36, 5224-5230, 1997.
- Chen, L., Han, D., Tao, J., and Su, L.: Overview of tropospheric NO<sub>2</sub> vertical column density retrieval from space measurement, *Journal of Remote Sensing*, 13, 343-360, 2009.
- Chen, L., Shang, H., Fan, M., Tao, J., Husi, L., Zhang, Y., Wang, H., Cheng, L., Zhang, X., and Wei, L.: Mission overview of the GF-5 satellite for atmospheric parameter monitoring, *National Remote Sensing Bulletin*, 25, 1917-1931, 2021.
- Coddington, O. M., Richard, E. C., Harber, D., Pilewskie, P., Woods, T. N., Chance, K., Liu, X., and Sun, K.: The TSIS-1 hybrid solar reference spectrum, *Geophys Res Lett*, 48, e2020GL091709, 2021.
- Cofano, A., Cigna, F., Santamaria Amato, L., Siciliani de Cumis, M., and Tapete, D.: Exploiting Sentinel-5P TROPOMI and ground sensor data for the detection of volcanic SO<sub>2</sub> plumes and activity in 2018–2021 at Stromboli, Italy, *Sensors-Basel*, 21, 6991, 2021.
- Corradino, C., Jouve, P., La Spina, A., and Del Negro, C.: Monitoring Earth's atmosphere with Sentinel-5 TROPOMI and Artificial Intelligence: Quantifying volcanic SO<sub>2</sub> emissions, *Remote Sens Environ*, 315, 114463, 2024.
- Cullis, C. F. and Hirschler, M. M.: Atmospheric Sulfur - Natural and Man-Made Sources, *Atmos Environ*, 14, 1263-1278, Doi 10.1016/0004-6981(80)90228-0, 1980.
- Eisinger, M. and Burrows, J. P.: Tropospheric sulfur dioxide observed by the ERS-2 GOME instrument, *Geophys Res Lett*, 25, 4177-4180, Doi 10.1029/1998gl900128, 1998.
- Finlayson-Pitts, B. J. and Pitts Jr, J. N.: Chemistry of the upper and lower atmosphere: theory, experiments, and applications, Elsevier 1999.
- Fioletov, V., McLinden, C. A., Griffin, D., Theys, N., Loyola, D. G., Hedelt, P., Krotkov, N. A., and Li, C.: Anthropogenic and volcanic point source SO<sub>2</sub> emissions derived from TROPOMI on board Sentinel-5 Precursor: first results, *Atmos Chem Phys*, 20, 5591-5607, 2020.
- Fioletov, V., McLinden, C., Krotkov, N., Yang, K., Loyola, D., Valks, P., Theys, N., Van Roozendael, M., Nowlan, C., and Chance, K.: Application of OMI, SCIAMACHY, and GOME-2 satellite SO<sub>2</sub> retrievals for detection of large emission



- 725 sources, *J Geophys Res-Atmos*, 118, 11,399-311,418, 2013.
- Fish, D. and Jones, R.: Rotational Raman scattering and the ring effect in zenith-sky spectra, *Geophys Res Lett*, 22, 811-814, 1995.
- Flynn, L. E., Seftor, C. J., Larsen, J. C., and Xu, P.: *The Ozone Mapping and Profiler Suite*, 2006.
- Global Volcanism Program, 2024. Report on Nyamuragira (DR Congo) (Sennert, S, ed.). Weekly Volcanic Activity Report, 6
- 730 November-12 November 2024. Smithsonian Institution and US Geological Survey.
- Global Volcanism Program, 2024. Report on Reykjanes (Iceland) (Sennert, S, ed.). Weekly Volcanic Activity Report, 21
- August-27 August 2024. Smithsonian Institution and US Geological Survey.
- Gottwald, M. and Bovensmann, H.: *SCIAMACHY-Exploring the changing Earth's Atmosphere*, Springer Science & Business Media 2010.
- 735 Grainger, J. and Ring, J.: Anomalous Fraunhofer line profiles, *Nature*, 193, 762-762, 1962.
- Heue, K. P., Brenninkmeijer, C. A. M., Wagner, T., Mies, K., Dix, B., Frieß, U., Martinsson, B. G., Slemr, F., and van Velthoven, P. F. J.: Observations of the 2008 Kasatochi volcanic SO<sub>2</sub> plume by CARIBIC aircraft DOAS and the GOME-2 satellite, *Atmos Chem Phys*, 10, 4699-4713, 10.5194/acp-10-4699-2010, 2010.
- Khokhar, M. F., Frankenberg, C., Van Roozendaal, M., Beirle, S., Kühl, S., Richter, A., Platt, U., and Wagner, T.: Satellite
- 740 observations of atmospheric SO<sub>2</sub> from volcanic eruptions during the time-period of 1996–2002, *Adv Space Res*, 36, 879-887, 10.1016/j.asr.2005.04.114, 2005.
- Kleipool, Q., Dobber, M., de Haan, J., and Levelt, P.: Earth surface reflectance climatology from 3 years of OMI data, *J Geophys Res-Atmos*, 113, 2008.
- Krotkov, N. A., Carn, S. A., Krueger, A. J., Bhartia, P. K., and Yang, K.: Band residual difference algorithm for retrieval of
- 745 SO<sub>2</sub> from the aura Ozone Monitoring Instrument (OMI), *IEEE Trans. Geosci. Remote Sensing*, 44, 1259-1266, Doi 10.1109/Tgrs.2005.861932, 2006.
- Krotkov, N. A., McLinden, C. A., Li, C., Lamsal, L. N., Celarier, E. A., Marchenko, S. V., Swartz, W. H., Bucsela, E. J., Joiner, J., and Duncan, B. N.: Aura OMI observations of regional SO<sub>2</sub> and NO<sub>2</sub> pollution changes from 2005 to 2015, *Atmos Chem Phys*, 16, 4605-4629, 2016.
- 750 Krotkov, N. A., McClure, B., Dickerson, R. R., Carn, S. A., Li, C., Bhartia, P. K., Yang, K., Krueger, A. J., Li, Z. Q., Levelt, P. F., Chen, H. B., Wang, P. C., and Lu, D. R.: Validation of SO<sub>2</sub> retrievals from the Ozone Monitoring Instrument over NE China, *J Geophys Res-Atmos*, 113, 259-269, ArtID16s40
- Doi 10.1029/2007jd008818, 2008.
- Krueger, A. J.: Sighting of El Chichón Sulfur Dioxide Clouds with the Nimbus 7 Total Ozone Mapping Spectrometer,
- 755 *Science*, 220, 1377-1379, DOI 10.1126/science.220.4604.1377, 1983.
- Kuttippurath, J., Patel, V. K., Pathak, M., and Singh, A.: Improvements in SO<sub>2</sub> pollution in India: role of technology and environmental regulations, *Environ Sci Pollut R*, 29, 78637-78649, 2022.
- Lee, C., Martin, R. V., van Donkelaar, A., O'Byrne, G., Krotkov, N., Richter, A., Huey, L. G., and Holloway, J. S.: Retrieval



- of vertical columns of sulfur dioxide from SCIAMACHY and OMI: Air mass factor algorithm development, validation, and  
760 error analysis, *J Geophys Res*, 114, 10.1029/2009jd012123, 2009.
- Levelt, P. F., Van den Oord, G. H. J., Dobber, M. R., Malkki, A., Visser, H., de Vries, J., Stammes, P., Lundell, J. O. V., and  
Saari, H.: The Ozone Monitoring Instrument, *IEEE Trans. Geosci. Remote Sensing*, 44, 1093-1101, Doi  
10.1109/Tgrs.2006.872333, 2006.
- Li, C., Joiner, J., Krotkov, N. A., and Bhartia, P. K.: A fast and sensitive new satellite SO<sub>2</sub> retrieval algorithm based on  
765 principal component analysis: Application to the ozone monitoring instrument, *Geophys Res Lett*, 40, 6314-6318, 2013.
- Lorente, A., Folkert Boersma, K., Yu, H., Dörner, S., Hilboll, A., Richter, A., Liu, M., Lamsal, L. N., Barkley, M., and De  
Smedt, I.: Structural uncertainty in air mass factor calculation for NO<sub>2</sub> and HCHO satellite retrievals, *Atmos Meas Tech*, 10,  
759-782, 2017.
- Mardani, M., Nowrouzi, M., and Abyar, H.: Assessing the environmental impact of offshore flares in the Persian Gulf: A  
770 comprehensive analysis of SO<sub>2</sub> emissions, *Advances in Environmental Technology*, 11, 63-74, 2025.
- Mccormick, M. P., Thomason, L. W., and Trepte, C. R.: Atmospheric effects of the Mt. Pinatubo eruption, *Nature*, 373, 399-  
404, Doi 10.1038/373399a0, 1995.
- Miller, T. P. and Casadevall, T. J.: Volcanic ash hazards to aviation, in: *Encyclopedia of Volcanoes*, edited by: Sigurdsson,  
H., Academic Press, San Diego, 915-930, 2000.
- 775 Munro, R., Eisinger, M., Anderson, C., Callies, J., Corpaccioli, E., Lang, R., Lefebvre, A., Livschitz, Y., and Albiñana, A. P.:  
GOME-2 on MetOp, *Proc. of The 2006 EUMETSAT Meteorological Satellite Conference*, Helsinki, Finland, 12—16 June,  
12-16,
- Newhall, C. G. and Self, S.: The volcanic explosivity index (VEI) an estimate of explosive magnitude for historical  
volcanism, *Journal of Geophysical Research: Oceans*, 87, 1231-1238, 1982.
- 780 Nowlan, C., Liu, X., Chance, K., Cai, Z., Kurosu, T., Lee, C., and Martin, R.: Retrievals of sulfur dioxide from the Global  
Ozone Monitoring Experiment 2 (GOME-2) using an optimal estimation approach: Algorithm and initial validation, *J  
Geophys Res-Atmos*, 116, 2011.
- Palmer, P. I., Jacob, D. J., Chance, K., Martin, R. V., Spurr, R. J., Kurosu, T. P., Bey, I., Yantosca, R., Fiore, A., and Li, Q.:  
Air mass factor formulation for spectroscopic measurements from satellites: Application to formaldehyde retrievals from the  
785 Global Ozone Monitoring Experiment, *J Geophys Res-Atmos*, 106, 14539-14550, 2001.
- Platt, U. and Stutz, J.: *Differential Optical Absorption Spectroscopy: Principles and Applications*, Physics of Earth and Space  
Environments, Springer, Verlag Berlin Heidelberg, 593 pp., 10.1007/978-3-540-75776-4 2008.
- Richter, A.: Algorithm Theoretical Basis Document for the GOME-2 Rapid Volcanic SO<sub>2</sub> product, SAVAA project.[Available  
at [https://www.iup.uni-bremen.de/doas/so2\\_alerts/gome2\\_so2\\_atbd\\_091005.pdf](https://www.iup.uni-bremen.de/doas/so2_alerts/gome2_so2_atbd_091005.pdf)], 2009.
- 790 Richter, A., Wittrock, F., and Burrows, J. P.: SO<sub>2</sub> measurements with SCIAMACHY, *Proc. Atmospheric Science Conference*,  
Frascati, Italy, 8 -12 May, 8-12,
- Rozanov, A., Rozanov, V., Buchwitz, M., Kokhanovsky, A., and Burrows, J.: SCIATRAN 2.0—A new radiative transfer



- model for geophysical applications in the 175–2400 nm spectral region, *Adv Space Res*, 36, 1015-1019, 2005.
- Seinfeld, J. H. and Pandis, S. N.: Atmospheric chemistry and physics: from air pollution to climate change, John Wiley & Sons 2016.
- Sinnhuber, B.-M., Sheode, N., Sinnhuber, M., Chipperfield, M., and Feng, W.: The contribution of anthropogenic bromine emissions to past stratospheric ozone trends: a modelling study, *Atmos Chem Phys*, 9, 2863-2871, 2009.
- Sioris, C. E. and Evans, W. F.: Filling in of Fraunhofer and gas-absorption lines in sky spectra as caused by rotational Raman scattering, *Appl Optics*, 38, 2706-2713, 1999.
- 795 Theys, N., De Smedt, I., Yu, H., Danckaert, T., van Gent, J., Hörmann, C., Wagner, T., Hedelt, P., Bauer, H., and Romahn, F.: Sulfur dioxide retrievals from TROPOMI onboard Sentinel-5 Precursor: algorithm theoretical basis, *Atmos Meas Tech*, 10, 119-153, 2017.
- Theys, N., Hedelt, P., De Smedt, I., Lerot, C., Yu, H., Vlietinck, J., Pedernana, M., Arellano, S., Galle, B., and Fernandez, D.: Global monitoring of volcanic SO<sub>2</sub> degassing with unprecedented resolution from TROPOMI onboard Sentinel-5  
805 Precursor, *Sci Rep-Uk*, 9, 2643, 2019.
- Theys, N., Fioletov, V., Li, C., De Smedt, I., Lerot, C., McLinden, C., Krotkov, N., Griffin, D., Clarisse, L., Hedelt, P., Loyola, D., Wagner, T., Kumar, V., Innes, A., Ribas, R., Hendrick, F., Vlietinck, J., Brenot, H., and Van Roozendael, M.: A sulfur dioxide Covariance-Based Retrieval Algorithm (COBRA): application to TROPOMI reveals new emission sources, *Atmos. Chem. Phys.*, 21, 16727-16744, 10.5194/acp-21-16727-2021, 2021.
- 810 Tilstra, L. G., de Graaf, M., Trees, V. J., Litvinov, P., Dubovik, O., and Stammes, P.: A directional surface reflectance climatology determined from TROPOMI observations, *Atmos Meas Tech*, 17, 2235-2256, 2024.
- Twomey, S.: The Influence of Pollution on the Shortwave Albedo of Clouds, *J Atmos Sci*, 34, 1149-1152, 10.1175/1520-0469(1977)034<1149:TIOPOT>2.0.CO;2, 1977.
- van Geffen, J. H. and van Oss, R. F.: Wavelength calibration of spectra measured by the Global Ozone Monitoring  
815 Experiment by use of a high-resolution reference spectrum, *Appl Optics*, 42, 2739-2753, 2003.
- Vandaele, A. C., Hermans, C., and Fally, S.: Fourier transform measurements of SO<sub>2</sub> absorption cross sections: II. Temperature dependence in the 29 000-44 000 cm<sup>-1</sup> (227-345 nm) region, *J Quant Spectrosc Ra*, 110, 2115-2126, DOI 10.1016/j.jqsrt.2009.05.006, 2009.
- Veefkind, J., Aben, I., McMullan, K., Förster, H., De Vries, J., Otter, G., Claas, J., Eskes, H., De Haan, J., and Kleipool, Q.:  
820 TROPOMI on the ESA Sentinel-5 Precursor: A GMES mission for global observations of the atmospheric composition for climate, air quality and ozone layer applications, *Remote Sens Environ*, 120, 70-83, 2012.
- Voors, R., De Vries, J., Bhatti, I. S., Lobb, D., Wood, T., Nick, V. D. V., Aben, I., and Veefkind, P.: TROPOMI, the Sentinel 5 precursor instrument for air quality and climate observations: status of the current design, *Society of Photo-optical Instrumentation Engineers*,
- 825 Vountas, M., Rozanov, V., and Burrows, J.: Ring effect: Impact of rotational Raman scattering on radiative transfer in Earth's atmosphere, *Journal of Quantitative Spectroscopy and Radiative Transfer*, 60, 943-961, 1998.





- Wagner, T., Burrows, J., Deutschmann, T., Dix, B., Von Friedeburg, C., Frieß, U., Hendrick, F., Heue, K.-P., Irie, H., Iwabuchi, H., Kanaya, Y., Keller, J., McLinden, C. A., Oetjen, H., Palazzi, E., Petritoli, A., Platt, U., Postylyakov, O., Pukite, J., Richter, A., van Roozendaal, M., Rozanov, A., Rozanov, V., Sinreich, R., Sanghavi, S., and Wittrock, F.: Comparison of box-air-mass-factors and radiances for Multiple-Axis Differential Optical Absorption Spectroscopy (MAX-DOAS) geometries calculated from different UV/visible radiative transfer models, *Atmos Chem Phys*, 7, 1809-1833, 2007.
- Wang, C., Wang, T., Wang, P., and Wang, W.: Assessment of the performance of TROPOMI NO<sub>2</sub> and SO<sub>2</sub> data products in the North China Plain: comparison, correction and application, *Remote Sens-Basel*, 14, 214, 2022.
- Wang, Q., Wang, Y., Xu, N., Mao, J., Sun, L., Shi, E., Hu, X., Chen, L., Yang, Z., and Si, F.: Preflight Spectral Calibration of the Ozone Monitoring Suite-Nadir on FengYun 3F Satellite, *Remote Sens-Basel*, 16, 1538, 2024.
- Yan, H., Wang, W., and Chen, L.: Temperature effects on the retrieval of SO<sub>2</sub> from ultraviolet satellite observations, *Remote Sensing of the Atmosphere, Clouds, and Precipitation V*, 379-386,
- Yan, H., Wang, H., Wang, W., and Zhang, X.: Volcanic SO<sub>2</sub> retrieved from GF-5 Environmental trace gas Monitoring Instrument, *National Remote Sensing Bulletin*, 25, 2326-2338, 10.11834/jrs.20210303, 2021.
- Yan, H., Li, X., Wang, W., Zhang, X., Chen, L., Han, D., Yu, C., and Gao, L.: Comparison of SO<sub>2</sub> column retrievals from BRD and DOAS algorithms, *Science China Earth Sciences*, 60, 1694-1706, 2017.
- Yang, K., Dickerson, R. R., Carn, S. A., Ge, C., and Wang, J.: First observations of SO<sub>2</sub> from the satellite Suomi NPP OMPS: Widespread air pollution events over China, *Geophys Res Lett*, 40, 4957-4962, 2013.
- Yang, K., Krotkov, N. A., Krueger, A. J., Carn, S. A., Bhartia, P. K., and Levelt, P. F.: Retrieval of large volcanic SO<sub>2</sub> columns from the Aura Ozone Monitoring Instrument: Comparison and limitations, *J Geophys Res*, 112, D24S43, doi: 10.1029/2007JD008825, 2007.
- Yang, K., Krotkov, N. A., Krueger, A. J., Carn, S. A., Bhartia, P. K., and Levelt, P. F.: Improving retrieval of volcanic sulfur dioxide from backscattered UV satellite observations, *Geophys Res Lett*, 36, 2009.
- Yang, K., Liu, X., Bhartia, P. K., Krotkov, N. A., Carn, S. A., Hughes, E. J., Krueger, A. J., Spurr, R. J., and Trahan, S. G.: Direct retrieval of sulfur dioxide amount and altitude from spaceborne hyperspectral UV measurements: Theory and application, *J Geophys Res-Atmos*, 115, 2010.
- Zhao, M., Si, F., Wang, Y., Zhou, H., Wang, S., Jiang, Y., and Liu, W.: First Year On-Orbit Calibration of the Chinese Environmental Trace Gas Monitoring Instrument Onboard GaoFen-5, *IEEE Trans. Geosci. Remote Sensing*, 58, 8531-8540, 2020.

855